Study of Charged–Current ep Interactions at $Q^2 > 200\,\mathrm{GeV}^2$ with the ZEUS Detector at HERA

ZEUS Collaboration

Abstract

Deep inelastic charged–current reactions have been studied in e^+p and e^-p collisions at a center of mass energy of about $300\,\mathrm{GeV}$ in the kinematic region $Q^2 > 200\,\mathrm{GeV}^2$ and $x > 0.006$ using the ZEUS detector at HERA. The integrated cross sections for $Q^2 > 200\,\mathrm{GeV}^2$ are found to be $\sigma_{e^+p \to \overline{\nu}X} = 30.3^{+5.5}_{-4.2}{}^{+1.6}_{-2.6}\,\mathrm{pb}$ and $\sigma_{e^-p \to \nu X} = 54.7^{+15.9}_{-\ 9.8}{}^{+2.8}_{-3.4}\,\mathrm{pb}$. Differential cross sections have been measured as functions of the variables x, y and Q^2. From the measured differential cross sections $d\sigma/dQ^2$, the W boson mass is determined to be $M_W = 79^{+8+4}_{-7-4}\,\mathrm{GeV}$. Measured jet rates and transverse energy profiles agree with model predictions. A search for charged–current interactions with a large rapidity gap yielded one candidate event, corresponding to a cross section of $\sigma_{e^+p \to \overline{\nu}X}(Q^2 > 200\,\mathrm{GeV}^2; \eta_{\max} < 2.5) = 0.8^{+1.8}_{-0.7} \pm 0.1\,\mathrm{pb}$.

The ZEUS Collaboration

M. Derrick, D. Krakauer, S. Magill, D. Mikunas, B. Musgrave, J.R. Okrasinski, J. Repond, R. Stanek, R.L. Talaga, H. Zhang
Argonne National Laboratory, Argonne, IL, USA [p]

M.C.K. Mattingly
Andrews University, Berrien Springs, MI, USA

P. Antonioli, G. Bari, M. Basile, L. Bellagamba, D. Boscherini, A. Bruni, G. Bruni, P. Bruni, G. Cara Romeo, G. Castellini[1], L. Cifarelli[2], F. Cindolo, A. Contin, M. Corradi, I. Gialas, P. Giusti, G. Iacobucci, G. Laurenti, G. Levi, A. Margotti, T. Massam, R. Nania, F. Palmonari, A. Pesci, A. Polini, G. Sartorelli, Y. Zamora Garcia[3], A. Zichichi
University and INFN Bologna, Bologna, Italy [f]

C. Amelung, A. Bornheim, J. Crittenden, R. Deffner, T. Doeker[4], M. Eckert, L. Feld, A. Frey[5], M. Geerts, M. Grothe, H. Hartmann, K. Heinloth, L. Heinz, E. Hilger, H.-P. Jakob, U.F. Katz, S. Mengel[6], E. Paul, M. Pfeiffer, Ch. Rembser, D. Schramm[7], J. Stamm, R. Wedemeyer
Physikalisches Institut der Universität Bonn, Bonn, Germany [c]

S. Campbell-Robson, A. Cassidy, W.N. Cottingham, N. Dyce, B. Foster, S. George, M.E. Hayes, G.P. Heath, H.F. Heath, D. Piccioni, D.G. Roff, R.J. Tapper, R. Yoshida
H.H. Wills Physics Laboratory, University of Bristol, Bristol, U.K. [o]

M. Arneodo[8], R. Ayad, M. Capua, A. Garfagnini, L. Iannotti, M. Schioppa, G. Susinno
Calabria University, Physics Dept.and INFN, Cosenza, Italy [f]

A. Caldwell[9], N. Cartiglia, Z. Jing, W. Liu, J.A. Parsons, S. Ritz[10], F. Sciulli, P.B. Straub, L. Wai[11], S. Yang[12], Q. Zhu
Columbia University, Nevis Labs., Irvington on Hudson, N.Y., USA [q]

P. Borzemski, J. Chwastowski, A. Eskreys, Z. Jakubowski, M.B. Przybycień, M. Zachara, L. Zawiejski
Inst. of Nuclear Physics, Cracow, Poland [j]

L. Adamczyk, B. Bednarek, K. Jeleń, D. Kisielewska, T. Kowalski, M. Przybycień, E. Rulikowska-Zarębska, L. Suszycki, J. Zając
Faculty of Physics and Nuclear Techniques, Academy of Mining and Metallurgy, Cracow, Poland [j]

Z. Duliński, A. Kotański
Jagellonian Univ., Dept. of Physics, Cracow, Poland [k]

G. Abbiendi[13], L.A.T. Bauerdick, U. Behrens, H. Beier, J.K. Bienlein, G. Cases, O. Deppe, K. Desler, G. Drews, M. Flasiński[14], D.J. Gilkinson, C. Glasman, P. Göttlicher, J. Große-Knetter, T. Haas, W. Hain, D. Hasell, H. Heßling, Y. Iga, K.F. Johnson[15], P. Joos, M. Kasemann, R. Klanner, W. Koch, U. Kötz, H. Kowalski, J. Labs, A. Ladage, B. Löhr, M. Löwe, D. Lüke, J. Mainusch[16], O. Mańczak, J. Milewski, T. Monteiro[17], J.S.T. Ng, D. Notz, K. Ohrenberg, K. Piotrzkowski, M. Roco, M. Rohde, J. Roldán, U. Schneekloth, W. Schulz, F. Selonke, B. Surrow, E. Tassi, T. Voß, D. Westphal, G. Wolf, U. Wollmer, C. Youngman, W. Zeuner
Deutsches Elektronen-Synchrotron DESY, Hamburg, Germany

H.J. Grabosch, A. Kharchilava[18], S.M. Mari[19], A. Meyer, S. Schlenstedt, N. Wulff
DESY-IfH Zeuthen, Zeuthen, Germany

G. Barbagli, E. Gallo, P. Pelfer
University and INFN, Florence, Italy [f]

G. Maccarrone, S. De Pasquale, L. Votano
INFN, Laboratori Nazionali di Frascati, Frascati, Italy [f]

I

A. Bamberger, S. Eisenhardt, T. Trefzger[20], S. Wölfle
Fakultät für Physik der Universität Freiburg i.Br., Freiburg i.Br., Germany [c]

J.T. Bromley, N.H. Brook, P.J. Bussey, A.T. Doyle, D.H. Saxon, L.E. Sinclair, M.L. Utley, A.S. Wilson
Dept. of Physics and Astronomy, University of Glasgow, Glasgow, U.K. [o]

A. Dannemann[21], U. Holm, D. Horstmann, R. Sinkus, K. Wick
Hamburg University, I. Institute of Exp. Physics, Hamburg, Germany [c]

B.D. Burow[22], L. Hagge[16], E. Lohrmann, G. Poelz, W. Schott, F. Zetsche
Hamburg University, II. Institute of Exp. Physics, Hamburg, Germany [c]

T.C. Bacon, N. Brümmer, I. Butterworth, V.L. Harris, G. Howell, B.H.Y. Hung, L. Lamberti[23], K.R. Long,
D.B. Miller, N. Pavel, A. Prinias[24], J.K. Sedgbeer, D. Sideris, A.F. Whitfield
Imperial College London, High Energy Nuclear Physics Group, London, U.K. [o]

U. Mallik, M.Z. Wang, S.M. Wang, J.T. Wu
University of Iowa, Physics and Astronomy Dept., Iowa City, USA [p]

P. Cloth, D. Filges
Forschungszentrum Jülich, Institut für Kernphysik, Jülich, Germany

S.H. An, G.H. Cho, B.J. Ko, S.B. Lee, S.W. Nam, H.S. Park, S.K. Park
Korea University, Seoul, Korea [h]

S. Kartik, H.-J. Kim, R.R. McNeil, W. Metcalf, V.K. Nadendla
Louisiana State University, Dept. of Physics and Astronomy, Baton Rouge, LA, USA [p]

F. Barreiro, J.P. Fernandez, R. Graciani, J.M. Hernández, L. Hervás, L. Labarga, M. Martinez, J. del Peso,
J. Puga, J. Terron, J.F. de Trocóniz
Univer. Autónoma Madrid, Depto de Física Teoríca, Madrid, Spain [n]

F. Corriveau, D.S. Hanna, J. Hartmann, L.W. Hung, J.N. Lim, C.G. Matthews[25], P.M. Patel, M. Riveline,
D.G. Stairs, M. St-Laurent, R. Ullmann, G. Zacek[25]
McGill University, Dept. of Physics, Montréal, Québec, Canada [a], [b]

T. Tsurugai
Meiji Gakuin University, Faculty of General Education, Yokohama, Japan

V. Bashkirov, B.A. Dolgoshein, A. Stifutkin
Moscow Engineering Physics Institute, Mosocw, Russia [l]

G.L. Bashindzhagyan[26], P.F. Ermolov, L.K. Gladilin, Yu.A. Golubkov, V.D. Kobrin, I.A. Korzhavina,
V.A. Kuzmin, O.Yu. Lukina, A.S. Proskuryakov, A.A. Savin, L.M. Shcheglova, A.N. Solomin, N.P. Zotov
Moscow State University, Institute of Nuclear Physics, Moscow, Russia [m]

M. Botje, F. Chlebana, J. Engelen, M. de Kamps, P. Kooijman, A. Kruse, A. van Sighem, H. Tiecke,
W. Verkerke, J. Vossebeld, M. Vreeswijk, L. Wiggers, E. de Wolf, R. van Woudenberg[27]
NIKHEF and University of Amsterdam, Netherlands [i]

D. Acosta, B. Bylsma, L.S. Durkin, J. Gilmore, C. Li, T.Y. Ling, P. Nylander, I.H. Park,
T.A. Romanowski[28]
Ohio State University, Physics Department, Columbus, Ohio, USA [p]

D.S. Bailey, R.J. Cashmore[29], A.M. Cooper-Sarkar, R.C.E. Devenish, N. Harnew, M. Lancaster[30],
L. Lindemann, J.D. McFall, C. Nath, V.A. Noyes[24], A. Quadt, J.R. Tickner, H. Uijterwaal,
R. Walczak, D.S. Waters, F.F. Wilson, T. Yip
Department of Physics, University of Oxford, Oxford, U.K. [o]

A. Bertolin, R. Brugnera, R. Carlin, F. Dal Corso, M. De Giorgi, U. Dosselli, S. Limentani, M. Morandin,
M. Posocco, L. Stanco, R. Stroili, C. Voci, F. Zuin
Dipartimento di Fisica dell' Universita and INFN, Padova, Italy [f]

II

J. Bulmahn, R.G. Feild[31], B.Y. Oh, J.J. Whitmore
Pennsylvania State University, Dept. of Physics, University Park, PA, USA [q]

G. D'Agostini, G. Marini, A. Nigro
Dipartimento di Fisica, Univ. 'La Sapienza' and INFN, Rome, Italy [f]

J.C. Hart, N.A. McCubbin, T.P. Shah
Rutherford Appleton Laboratory, Chilton, Didcot, Oxon, U.K. [o]

E. Barberis, T. Dubbs, C. Heusch, M. Van Hook, W. Lockman, J.T. Rahn, H.F.-W. Sadrozinski,
A. Seiden, D.C. Williams
University of California, Santa Cruz, CA, USA [p]

J. Biltzinger, R.J. Seifert, O. Schwarzer, A.H. Walenta
Fachbereich Physik der Universität-Gesamthochschule Siegen, Germany [c]

H. Abramowicz, G. Briskin, S. Dagan[32], A. Levy[26]
School of Physics, Tel-Aviv University, Tel Aviv, Israel [e]

J.I. Fleck[33], M. Inuzuka, T. Ishii, M. Kuze, S. Mine, M. Nakao, I. Suzuki, K. Tokushuku,
K. Umemori, S. Yamada, Y. Yamazaki
Institute for Nuclear Study, University of Tokyo, Tokyo, Japan [g]

M. Chiba, R. Hamatsu, T. Hirose, K. Homma, S. Kitamura[34], T. Matsushita, K. Yamauchi
Tokyo Metropolitan University, Dept. of Physics, Tokyo, Japan [g]

R. Cirio, M. Costa, M.I. Ferrero, S. Maselli, C. Peroni, R. Sacchi, A. Solano, A. Staiano
Universita di Torino, Dipartimento di Fisica Sperimentale and INFN, Torino, Italy [f]

M. Dardo
II Faculty of Sciences, Torino University and INFN - Alessandria, Italy [f]

D.C. Bailey, F. Benard, M. Brkic, C.-P. Fagerstroem, G.F. Hartner, K.K. Joo, G.M. Levman, J.F. Martin,
R.S. Orr, S. Polenz, C.R. Sampson, D. Simmons, R.J. Teuscher
University of Toronto, Dept. of Physics, Toronto, Ont., Canada [a]

J.M. Butterworth, C.D. Catterall, T.W. Jones, P.B. Kaziewicz, J.B. Lane, R.L. Saunders, J. Shulman,
M.R. Sutton
University College London, Physics and Astronomy Dept., London, U.K. [o]

B. Lu, L.W. Mo
Virginia Polytechnic Inst. and State University, Physics Dept., Blacksburg, VA, USA [q]

W. Bogusz, J. Ciborowski, J. Gajewski, G. Grzelak[35], M. Kasprzak, M. Krzyżanowski,
K. Muchorowski[36], R.J. Nowak, J.M. Pawlak, T. Tymieniecka, A.K. Wróblewski, J.A. Zakrzewski,
A.F. Żarnecki
Warsaw University, Institute of Experimental Physics, Warsaw, Poland [j]

M. Adamus
Institute for Nuclear Studies, Warsaw, Poland [j]

C. Coldewey, Y. Eisenberg[32], D. Hochman, U. Karshon[32], D. Revel[32], D. Zer-Zion
Weizmann Institute, Nuclear Physics Dept., Rehovot, Israel [d]

W.F. Badgett, J. Breitweg, D. Chapin, R. Cross, S. Dasu, C. Foudas, R.J. Loveless, S. Mattingly,
D.D. Reeder, S. Silverstein, W.H. Smith, A. Vaiciulis, M. Wodarczyk
University of Wisconsin, Dept. of Physics, Madison, WI, USA [p]

S. Bhadra, M.L. Cardy, W.R. Frisken, M. Khakzad, W.N. Murray, W.B. Schmidke
York University, Dept. of Physics, North York, Ont., Canada [a]

IV

1 Introduction

In comparison to fixed target neutrino scattering experiments [1], the HERA ep collider extends the kinematic region for studying charged–current (CC) deep inelastic scattering (DIS) by about two orders of magnitude in Q^2. In addition, HERA allows measurements of CC DIS at lower x ($x < 0.01$). Here Q^2 is the negative square of the four–momentum transferred between the electron[1] and the proton, and x is the Bjorken scaling variable.

Both the H1 [2] and ZEUS [3] collaborations have previously reported cross section measurements for the process $e^- p \to \nu_e X$, where X denotes the hadronic final state. These investigations, based on the data collected in 1993, established that the Q^2 dependence of the CC cross section is consistent with that of the W propagator and that the CC and neutral–current (NC) cross sections have similar magnitude for $Q^2 \gtrsim M_W^2$ (M_W denotes the W mass). The H1 collaboration has also measured the integrated cross section [4] and the differential cross section $d\sigma/dQ^2$ [5] for $e^+ p \to \overline{\nu}_e X$ with missing transverse momentum ($\not{P}_t$) above 25 GeV.

In 1994 ZEUS has collected $2.93\,\mathrm{pb}^{-1}$ of $e^+ p$ data and $0.27\,\mathrm{pb}^{-1}$ of $e^- p$ data in collisions of 820 GeV protons with 27.5 GeV electrons. In order to study both e^+ and e^- induced CC reactions, these data samples have been combined with the $0.55\,\mathrm{pb}^{-1}$ of $e^- p$ data taken in 1993 with an electron beam energy of 26.7 GeV [3].

In the quark parton model (including the leading order QCD evolution in Q^2), the unpolarized $e^+ p$ and $e^- p$ charged–current differential cross sections are:[2]

$$\frac{d^2\sigma_{e^+ p \to \overline{\nu} X}}{dx dQ^2} = \frac{G_F^2}{2\pi} \left(\frac{M_W^2}{M_W^2 + Q^2} \right)^2 \sum_{i=1}^{2} \left[x\overline{u}_i(x, Q^2) + (1-y)^2 \, x d_i(x, Q^2) \right] , \qquad (1)$$

$$\frac{d^2\sigma_{e^- p \to \nu X}}{dx dQ^2} = \frac{G_F^2}{2\pi} \left(\frac{M_W^2}{M_W^2 + Q^2} \right)^2 \sum_{i=1}^{2} \left[x u_i(x, Q^2) + (1-y)^2 \, x \overline{d}_i(x, Q^2) \right] , \qquad (2)$$

where u_i and d_i are the densities of up–type and down–type quarks of the ith generation in the proton, G_F is the Fermi coupling constant, and y is the fractional energy transfer to the proton in its rest system. The factor $(1-y)^2$, which suppresses the quark (antiquark) contribution to the $e^+ p$ ($e^- p$) cross section, is a direct consequence of the $V-A$ structure of the weak coupling.

As equations 1 and 2 show, the charged current couples to different quark flavors for e^+ and e^- beams and the valence and sea contributions have very different y dependences. In addition, the Q^2 dependence of the cross section allows a measurement of the W propagator effect and thus a determination of the W mass in the space–like region, complementing the measurements of direct W production at $p\overline{p}$ colliders [6].

This paper reports on measurements of the integrated and differential cross sections for both $e^+ p$ and $e^- p$ CC DIS in the kinematic region $Q^2 > 200\,\mathrm{GeV}^2$. The differential cross sections were measured as functions of x, y and Q^2, where the latter dependence was

---

[1]In the following, "electron" is generically used to denote both electrons and positrons.

[2]For the current integrated luminosity, any contributions to the CC cross section from hard subprocesses involving 3rd generation quarks (b, t) can be neglected. In this approximation the relation between quark densitites and CC structure functions is given by $F_2^{e^+ p \to \overline{\nu} X} \propto d + s + \overline{u} + \overline{c}$, $F_2^{e^- p \to \nu X} \propto u + c + \overline{d} + \overline{s}$, $x F_3^{e^+ p \to \overline{\nu} X} \propto d + s - \overline{u} - \overline{c}$ and $x F_3^{e^- p \to \nu X} \propto u + c - \overline{d} - \overline{s}$.

used to determine the W mass. The available statistics allowed studies of the hadronic final state at high Q^2 in CC DIS: the jet rates and transverse energy jet profiles were determined and compared to Monte Carlo predictions. The number of events with two jets (plus the proton remnant) directly measures the rate of hard QCD subprocesses.

Recently, diffractive NC DIS has received particular attention [7]–[10]. These reactions are characterized by an absence of final state particles in a wide rapidity interval between the outgoing proton system (which escapes through the forward beam hole) and the rest of the hadronic final state. Such a rapidity gap results in a quiet region in the forward part of the main detector. Diffractive CC reactions are interesting because they predominantly occur at high Q^2 and also because they provide the possibility to study the flavor content of the states exchanged between proton and W boson. A search for events with a rapidity gap in our CC samples yielded one candidate, which will be described in detail. The rate of large rapidity gap CC events was compared to model predictions and to the NC case. After a brief summary of the experimental setup in section 2, the kinematics and the selection of CC events are described in section 3. The cross section calculations and the evaluation of the systematic uncertainties are outlined in section 4. Finally, section 5 contains the results, which are summarized in section 6.

2   Experimental Setup

In 1994, a total of 153 colliding bunches were stored in the electron and the proton beams of HERA, together with an additional 17 proton and 15 electron non–colliding bunches which were used to study beam induced backgrounds. The r.m.s. bunch length was about 20 cm for protons and 1 cm for electrons, resulting in an event vertex position distribution[3] with an r.m.s. width of 12 cm in Z. The typical instantaneous luminosity was $1.5 \cdot 10^{30} \, \text{cm}^{-2} \, \text{s}^{-1}$. The following description refers to the 1994 running period. Details of the 1993 experimental setup and HERA running conditions can be found in [11].

2.1   The ZEUS Detector

A description of the ZEUS detector is available in [12, 13]. The primary components used in this analysis were the uranium–scintillator calorimeter [14] and the central tracking detectors.

The calorimeter is divided into three parts, forward (FCAL) covering the polar angle[4] interval $2.6° < \theta < 37°$, the barrel (BCAL, $37° < \theta < 129°$) and rear (RCAL, $129° < \theta < 176.1°$). The calorimeters are subdivided into towers which subtend solid angles between 0.006 and 0.04 steradians. Each tower is longitudinally segmented into electromagnetic (EMC) and two hadronic (HAC) sections (one in RCAL). The electromagnetic layer of each tower is further subdivided transversely into four cells (two in RCAL). The total number of cells is 2172, 2592 and 1154 in FCAL, BCAL and RCAL, respectively. Under test beam conditions, the calorimeter has an energy resolution of $\sigma_E/E = 18\%/\sqrt{E(\text{GeV})}$ for electrons and $\sigma_E/E = 35\%/\sqrt{E(\text{GeV})}$ for hadrons. The time resolution is below 1 ns for energy deposits greater than 4.5 GeV.

---

[3]The ZEUS coordinate system is right–handed with the Z axis pointing in the proton direction, hereafter referred to as forward, and the X axis horizontal, pointing towards the center of HERA.

[4]The polar angle θ is defined here with respect to the nominal interaction point.

Energy which penetrates through the CAL can be measured in the Backing Calorimeter (BAC) which consists of proportional chambers interleaved with the iron plates which form the return yoke of the solenoid [15].[5]

The tracking system consists of a vertex detector [16] and a central tracking chamber (CTD) [17] operating in a 1.43 T magnetic field parallel to the beam axis. The polar angle region in which the CTD allows accurate momentum measurement is $15°<\theta<164°$. The transverse momentum resolution for full length tracks is $\sigma(p_t)/p_t = [0.005 p_t (\text{GeV})] \oplus 0.016$. The luminosity was measured by the rate of high energy photons from the process $ep \rightarrow ep\gamma$ detected in a lead–scintillator calorimeter [18] located at $Z = -107$ m.

2.2   Trigger Configuration

Data were collected with a three–level trigger system [13]. The first–level trigger conditions used in this analysis were based on electromagnetic energy, transverse energy, and missing transverse energy in the calorimeter. The thresholds were significantly below the corresponding cuts applied in the subsequent selection. The second level trigger rejected backgrounds (mostly p–gas interactions and cosmic rays) for which the calorimeter timing was inconsistent with an ep interaction. Events were accepted as CC candidates if the following conditions were all fulfilled:

1. The missing transverse momentum $\not{P}_t$ exceeded 9 GeV (see equation 3).

2. $\not{P}_t$ evaluated from all calorimeter cells except those adjacent to the forward beam pipe exceeded 8 GeV.

3. Either a track was found in the CTD or at least 10 GeV was deposited in the FCAL.

The third–level trigger applied stricter timing cuts and also pattern recognition algorithms to reject cosmic rays.

2.3   Monte Carlo Simulation

Simulated CC DIS events with electroweak radiative corrections were generated using LEPTO [19] interfaced to HERACLES [20] via DJANGO [21]. The MRSA set of NLO parton density parameterizations was used, which is based on preliminary 1993 F_2 measurements by ZEUS and H1 as well as on recent data on W asymmetries from CDF and on Drell–Yan cross sections (cf. [22] and the references therein). The latter measurements constrain the difference $\overline{u} - \overline{d}$, to which CC reactions are particularly sensitive. The hadronic final state was simulated using the color–dipole model as implemented in ARIADNE [23] for the QCD cascade and JETSET [24] for the hadronization. In addition, MC samples using the MEPS option of LEPTO instead of ARIADNE were generated. Each of the CC MC samples contained about 10^4 events. The results were corrected for radiative effects using these CC MC sets[6].

MC samples of NC DIS and photoproduction events were employed to simulate backgrounds to CC DIS. For the NC DIS simulation the same programs were used as for

---

[5]Due to the present limited understanding of the Monte Carlo simulation of energy deposits in the BAC, this component has been used only for systematic checks in this analysis.

[6]All kinematic quantities are inferred from the four–momentum of the propagator.

the CC events. Samples of both direct and resolved photoproduction events were generated using both PYTHIA [24] and HERWIG [25]. Photoproduction of $c\bar{c}$ and $b\bar{b}$ pairs was simulated using both PYTHIA and AROMA [26].

To calculate efficiencies for diffractive CC interactions the POMPYT [27] Monte Carlo program was used. This program is based on the factorizing model of Ingelman and Schlein [28] and assumes a hard quark density in the pomeron which satisfies the momentum sum rule.

All simulated events were passed through a GEANT based [29] detector simulation and processed with the same analysis programs as the data.

3   Kinematics and Event Selection

In CC ep reactions the final state neutrino remains undetected. This fact imposed special conditions both for the reconstruction of kinematic variables and for the event selection.

3.1   Kinematic Variables

The kinematics of the interaction $ep \to \nu X$ are defined by the four–momenta k and P of the incident electron and proton respectively, and the four–momentum of the final state neutrino (k') or the final state hadronic system (P'). The four–momentum transfer between the electron and the proton is given by $q = k - k' = P' - P$.

In addition to $s = (k + P)^2$, the square of the ep center of mass energy, three Lorentz invariants are defined in terms of these four–momenta:

- $Q^2 = -q^2$, the negative square of the four–momentum transfer,

- $x = \dfrac{Q^2}{2q \cdot P}$, the Bjorken scaling variable,

- $y = \dfrac{q \cdot P}{k \cdot P}$, the fractional energy transfer to the proton in its rest system.

Neglecting mass terms, these variables are related by $Q^2 = x\,y\,s$.

The Jacquet–Blondel method [30] was used to reconstruct the kinematic variables from the measured missing transverse momentum,

$$\not{P}_t = \sqrt{\left(\sum_i p_X^i\right)^2 + \left(\sum_i p_Y^i\right)^2} \, , \tag{3}$$

and the quantity δ, given by

$$\delta = \sum_i \left(E^i - p_Z^i\right) \, , \tag{4}$$

where the sums run over all EMC (HAC) cells with energy deposits E^i above 60 MeV (110 MeV) and the $\vec{p}^{\,i}$ are the momenta assigned to each calorimeter cell (calculated assuming zero mass and using the geometrical cell center and the measured vertex position). The Jacquet–Blondel estimators of y, Q^2 and x are given by

$$y_{JB} = \frac{\delta}{2E_e} \, , \qquad Q^2_{JB} = \frac{\not{P}_t^{\,2}}{1 - y_{JB}} \, , \qquad x_{JB} = \frac{\not{P}_t^{\,2}}{s\,y_{JB}(1 - y_{JB})} \, , \tag{5}$$

where E_e is the electron beam energy.

3.2 Selection of Charged–Current Events

The number of CC triggers was about 10^5, almost entirely due to p–gas interactions, cosmic rays, and beam halo muons. After a preselection which required a tracking vertex and stricter timing cuts than at the trigger level, about 6300 e^+p and 1500 e^-p candidates remained (cf. table 1). In the following, we describe the cuts which were applied to extract the CC signal. Table 1 gives the numbers of events remaining after each selection cut, as well as the corresponding efficiencies estimated using the ARIADNE MC samples.

The following conditions were imposed on all events passing the trigger:

- $\not{P}_t > 11\,\text{GeV}$ was required. The trigger simulation indicated that this cut was sufficiently far above the 9 GeV trigger threshold to ensure high trigger efficiency.

- The events had to have a tracking vertex with $|Z_{\text{vtx}}| < 45\,\text{cm}$, where $Z_{\text{vtx}} = 0$ at the nominal interaction point. This cut eliminated a large fraction of non–ep background.

- $\not{P}_t^{\text{out}}/\not{P}_t > 0.6$ was required, where $\not{P}_t^{\text{out}}$ is the net transverse momentum for all calorimeter cells with a polar angle above $9°$ with respect to the nominal vertex position. This cut rejected p–gas and p–beampipe collisions, for which $\not{P}_t$ is concentrated at small polar angles.

- There had to be at least one reconstructed track originating from the vertex, which had a polar angle between $15°$ and $164°$ and a transverse momentum exceeding 0.2 GeV. This requirement removed cosmic ray events and p–gas interactions with spurious vertices caused by low–energy secondary interactions in the beam pipe.

- The difference $\Delta\phi$ between the azimuth of the net transverse momentum as measured by the CTD tracks with polar angle between $15°$ and $164°$, and the azimuth measured by the calorimeter, was required to fulfill $|\Delta\phi| < 1\,\text{rad}$. This requirement removed overlays of cosmic rays on ep–interactions.

- In addition, a pattern recognition algorithm based on the topology of the calorimeter energy distribution was applied to reject cosmic rays and beam halo muons.

Simulation of backgrounds due to NC DIS and photoproduction interactions showed that such events passing the above cuts were concentrated at low $\not{P}_t$. The same was found for the non–ep background. Hence the following additional cuts were applied to events with $\not{P}_t < 30\,\text{GeV}$:

- $y_{JB} < 0.8$, which reduced NC DIS background.

- $\not{P}_t/E_t > 0.4$, where $E_t = \sum_i \sqrt{(p_X^i)^2 + (p_Y^i)^2}$ is the total transverse energy. This cut demanded an azimuthally collimated energy flow and rejected photoproduction and also p–gas background.

- $P_t^{\text{tracks}}/\not{P}_t > 0.1$, where $P_t^{\text{tracks}} = \sqrt{\left(\sum_j P_X^{\text{track}\,j}\right)^2 + \left(\sum_j P_Y^{\text{track}\,j}\right)^2}$ and j runs over all vertex–fitted tracks with polar angle between $15°$ and $164°$. This cut effectively tightened the $\not{P}_t^{\text{out}}/\not{P}_t$ requirement (cf. above) and also removed events with additional non–ep related energy deposits in the calorimeter (mainly cosmic rays).

The resulting sample was visually scanned and 3 non–ep background events were identified in the e^+p sample and removed (all were overlays of muons and p–gas reactions). No non–ep background was found in the e^-p sample. The distribution in x and Q^2 of the final samples of 56 e^+p events and 30 e^-p events is shown in figure 1.

3.3 The Neutral–Current Control Sample

The acceptance corrections and the methods of reconstructing the kinematic variables were based on the MC simulation described in section 2.3. In order to verify the accuracy of the simulation, several systematic checks were performed using a sample[7] of high–Q^2 NC events selected as follows:

- As in the CC case (cf. section 2.2), the NC trigger requirements were based on the calorimeter energy deposits. The same timing cuts were applied as for the CC trigger. Photoproduction background was efficiently suppressed by the cut $\delta > 25\,\mathrm{GeV}$ (cf. eq. 4).

- In the offline NC selection, an electron candidate with at least $10\,\mathrm{GeV}$ energy had to be identified by a neural–network algorithm using the pattern of the calorimeter energy deposits [31]. The electron had to be isolated (less than $2\,\mathrm{GeV}$ of energy not associated with the electron in an (η, ϕ)–cone[8] of radius $R = 0.5$ centered on the electron direction) and had to have a matching track if it was in the region $20° < \theta < 160°$. In addition, the event had to have a reconstructed tracking vertex, and satisfy $35\,\mathrm{GeV} < \delta < 65\,\mathrm{GeV}$ and $Q^2 > 200\,\mathrm{GeV}^2$, where Q^2 was reconstructed using the double angle (DA) method [32].

- For the selected NC events, the track(s) and the calorimeter deposits associated with the electron were deleted from the data, and the reconstruction of the event vertex was repeated.

- These modified NC events were then processed through the complete CC analysis chain. In order to account for the different cross sections, a weight

$$
w = \frac{d\sigma_{e^+p\to\overline{\nu}X}/dx\,dQ^2}{d\sigma_{e^+p\to e^+X}/dx\,dQ^2} \quad \text{for } e^+p \qquad \text{resp.} \qquad w = \frac{d\sigma_{e^-p\to\nu X}/dx\,dQ^2}{d\sigma_{e^-p\to e^-X}/dx\,dQ^2} \quad \text{for } e^-p
$$

  was assigned to each event, where leading order differential cross sections, evaluated at x and Q^2 as reconstructed by the double angle method, were used.

  After the CC selection, 2269 e^+p and 167 e^-p events with $Q^2 > 200\,\mathrm{GeV}^2$ remained, where Q^2 was reconstructed as described in section 4.1. The respective sums of weights were 50.8 and 6.2.

The control sample was not corrected for the efficiency of the NC event selection, for remaining backgrounds, or for migrations due to mismeasurement of x and Q^2. The distributions of Q^2_{JB}, x_{JB}, y_{JB} and $\not{P}_t$ agreed sufficiently well with the corresponding CC MC distributions to allow for quantitative checks of the efficiency calculations and correction methods.

---

[7]Data collected in 1994 were used.
[8]The pseudorapidity η is defined as $-\ln[\tan(\theta/2)]$, where θ is the polar angle with respect to the proton beam direction, taken from the reconstructed interaction point.

4 Cross Section Evaluation

The integrated and differential cross sections were calculated from the observed numbers of events and the integrated luminosity after subtracting the estimated photoproduction background and correcting for detection efficiencies and migrations.

The e^-p data from 1993 and 1994 were combined by appropriately weighting the 1993 event numbers in each individual bin under consideration. The weights, which account for slight differences in the electron beam energies and in the trigger and detector configurations, were in the range between 0.95 and 1.05.

All statistical errors have been evaluated using the observed numbers of events and asymmetric Poisson confidence intervals.

4.1 Reconstruction of Kinematic Variables

Due to the energy loss of the hadrons in inactive material in the central detector, the calorimeter measurement underestimated both $\not{P}_t$ and δ. The detector simulation was used to derive corrected values $\not{P}_{t\,\mathrm{cor}}$ and y_{cor}, as second–order polynomials of the respective raw values $\not{P}_t$ and y_{JB}, where the coefficients for the y correction depend on $\not{P}_t$. The correction of $\not{P}_t$ was about 20% at low $\not{P}_t$, decreasing to $\approx 10\%$ for $\not{P}_t \gtrsim 50\,\mathrm{GeV}$; in y, the corrections were highest for $y \approx 0.1$ and low $\not{P}_t$ ($\approx 20\%$), decreasing with both increasing y and increasing $\not{P}_t$. The corrected values $Q^2{}_{\mathrm{cor}}$ and x_{cor} were calculated in terms of $\not{P}_{t\,\mathrm{cor}}$ and y_{cor} using equation 5.

The correction was tested using the NC control sample (cf. section 3.3) by evaluating the means and widths of the distributions of $\delta A = (A_{\mathrm{cor}} - A_{DA})/A_{DA}$ for $A = Q^2, x$ or y in all intervals of these variables (cf. section 4.2). Typically, the mean values were below 10% for x and Q^2 and below 5% for y; the r.m.s. widths were roughly 20% for x, 25% for Q^2, and 10% for y. In the highest x and Q^2 bins, these estimates are based on only a few NC events and hence are of limited statistical significance.

4.2 Choice of Intervals

The kinematic ranges of the variables x, y and Q^2 covered by this analysis are $x{>}0.006$, $0{<}y{<}1$ and $Q^2{>}200\,\mathrm{GeV}^2$. For the measurement of differential cross sections in x and Q^2, equal bins in $\log(x)$ and $\log(Q^2)$ respectively were used (see tables 2, 3 and 4). The y range was subdivided in 5 equal intervals. These choices of bins provided roughly equal numbers of events in all intervals and ensured that the intervals were much wider than the experimental resolutions and the systematic shifts described in section 4.1.

4.3 Background Subtraction

The contamination from NC events, estimated using a LEPTO Monte Carlo sample [19], was negligible. The background from photoproduction processes was determined by applying the selection algorithm to photoproduction events, simulated with HERWIG, which had transverse energy $E_t > 20\,\mathrm{GeV}$ (E_t being determined from the momenta of all final state particles). While the simulated photoproduction events which passed the CC selection all had $E_t > 30\,\mathrm{GeV}$, they were concentrated at low $\not{P}_t$. The estimated photoproduction contamination in the lowest bins of x and Q^2 was $\sim 15\%$.

No event passing the CC selection was found in the MC samples simulating heavy quark photoproduction, yielding an upper limit on the cross section for this background of less than 0.2% of the CC cross section. The heavy quark background is therefore neglected. No subtraction has been applied for non–ep background (cosmic and beam halo muons, p–gas reactions, and overlays of such events with ep reactions). This background is negligible after event selection and visual scanning (cf. section 3.2).

4.4 Acceptance Correction and Unfolding

Bin–to–bin migrations and the efficiencies of trigger and selection cuts were taken into account using a bin–by–bin correction method, where the correction factors were calculated from the Monte Carlo simulation described in section 2. Typical acceptance corrections range from 40% to 80%, with an average of about 60% (cf. tables 1 and 2 to 5). The statistical errors of the correction factors were about 10 times smaller than the statistical errors of the data and have been neglected. In addition to the acceptance corrections, ζ, defined as the ratio of the number of events reconstructed in a given bin to the number of events generated in the same bin, tables 2 to 5 also show the purities, ξ, defined as the fraction of the events reconstructed in a given bin which were also generated in the same bin.

The efficiency calculation was checked using the NC control sample. Both the overall acceptances and those of individual cuts (cf. table 1) typically agreed with the MC values within 5%.

The bin–by–bin unfolding procedure described above was cross checked by applying a single step matrix unfolding based on Bayes' theorem [33]. The off–diagonal elements of the unfolding matrix were usually less than 25% of the corresponding diagonal elements, indicating that migrations between bins were small. In cases where the data are poorly modeled by the MC or where migrations play a dominant rôle, the two methods are expected to yield significantly different results. The resulting differences were however found to be well below the statistical errors. They are included in the systematic uncertainties (cf. tables 2 and 3).

4.5 Systematic Uncertainties

In the following, we summarize the studies which were performed in order to estimate the systematic uncertainties. For the case of $d\sigma/dQ^2$, the dominant systematic uncertainties are detailed in tables 2 and 3. The remaining systematic errors were all below 5% and typically below 1%. Where appropriate, independent checks of systematic uncertainties have been calculated using the NC control sample. The systematic deviations observed in this sample agreed well with the values quoted below.

- In the detector simulation, the calorimeter energy scale was varied by $\pm 3\%$ ($\pm 5\%$ in the FCAL), corresponding to the level at which it is currently understood. Using the BAC it was checked that this variation also covers possible effects due to energy leakage out of the CAL. Using the BAC energy deposits to correct jet energies in CC events increased $\not{P}_t$ by about 2% on average.

  Such an energy scale uncertainty gives rise to uncertainties in the cross section which are typically between 5% and 10%, but can be up to 30% in the highest Q^2 and y bins.

8

- The systematic uncertainty of the photoproduction background subtraction was estimated as the quadratic sum of its statistical error and an additional $\pm 50\%$ uncertainty which accounted for differences between E_t and $\not{P}_t/E_t$ spectra of photoproduction data and MC.

  The uncertainty of the background estimate mainly affected the lowest Q^2 and x bins. It was the dominant systematic error in the lowest x bin for e^+p reactions.

- The reconstruction of the kinematic variables was modified in the following way: in each bin[9] of $A = \not{P}_t$ or y the reconstructed values of $\not{P}_t$ and y were multiplied with $1/(1 + \langle \delta A \rangle)$ (cf. section 4.1), where δA was averaged over the weighted NC control sample events in this bin. This corresponded to correcting on average to the DA values as derived from the NC control sample. Q^2, x and y were calculated from the resulting values using equations 5. This changed the measured cross sections by 10% or less, except in the lowest and highest Q^2 bins, where variations of up to 15% were seen.

- In order to check the simulation of the tracking, the combined acceptance of all cuts using tracking information was evaluated for the NC control sample, in each interval of Q^2, x and y, both for data and for simulated NC events. The data/MC ratio of these acceptances was found to be consistent with unity. In almost all bins the deviation was less than 3%, which was used as the overall systematic uncertainty.

- A one step Bayes unfolding was used instead of the bin–by–bin unfolding (cf. discussion in section 4.4). This variation caused uncertainties of $10 - 15\%$ in the lowest and the highest bins of Q^2, x and y (-25% in the highest y bin for e^+p).

- In the trigger simulation, the first level trigger thresholds were increased to a level where the measured trigger efficiencies were close to 100%. Except in the lowest Q^2 bins, where effects up to 4% were observed, this had a negligible effect indicating that the efficiency calculations were insensitive to the detailed shape of the trigger turn–on curves.

- In order to test the sensitivity to the details of the parton shower simulation, the MEPS model was used instead of the ARIADNE MC for calculating acceptance corrections and for unfolding. This affected the cross section results only negligibly.

  In addition, the selection cuts on $\not{P}_t$, $\Delta\phi$, the track requirements, and the cuts at low $\not{P}_t$ have been varied using the MEPS MC sample instead of the data, and the ARIADNE sets for acceptance corrections and unfolding. This tested whether the simulated shapes of the relevant distributions differ in the vicinities of these cuts.

  Each of the cut variations changed the results by less than typically 1%, except the $\not{P}_t$ variation in the lowest x and Q^2 bins (up to 5%) and the track requirement (up to 3% in some bins).

- Different parton distribution functions (MRSD0 [34], MRSD$'_-$ [35], GRV [36] and CTEQ 2pM [37]) were used in the MC samples used for the acceptance corrections.[10] The resulting variations were small and have been neglected.

---

[9]For $\not{P}_t$, the bin boundaries were $0 - 20 - 30 - 40 - 50 - \infty$ GeV.

[10]The most significant variation of the Standard Model cross section prediction due to parton distributions is seen in $d\sigma/dx$ at $0.01 \lesssim x \lesssim 0.1$ (cf. section 5.1).

The overall systematic uncertainty for each result (including ratios of cross sections and the W mass) was calculated by evaluating the variation of this result due to each of the modifications of the analysis procedure described above (including the luminosity uncertainties of $\pm 2.0\%$ for the e^+p sample and $\pm 3.0\%$ for the e^-p sample) and then separately summing in quadrature the positive and negative deviations.

5   Results

The results will be presented in three sections: cross sections and the determination of M_W, jet rates and profiles, and finally the search for events with a large rapidity gap. The abbreviation 'SM' (for Standard Model) is used to indicate the theoretical predictions. Unless otherwise noted, these were estimated using LEPTO and the MRSA parton distributions. The propagator four–momentum was used to calculate kinematic quantitites.

5.1   Cross Sections and Cross Section Ratios

Differential cross sections as functions of Q^2, x and y

The values of the cross section, σ_i, in bins of Q^2, for e^+p and e^-p data, are listed in tables 2 and 3 respectively. Also shown are the dominant systematic errors as described in section 4.5. The results are plotted in figure 2a, where the SM predictions are also shown.

The results for $Q^2 > 200\,\mathrm{GeV}^2$ in bins of x and y are given in tables 4 and 5. The differential CC cross sections are shown in figures 3a and 4a together with the corresponding SM predictions.

Figures 2b, 3b and 4b show the ratios $\sigma_{e^+p \to \overline{\nu}X}/\sigma_{e^-p \to \nu X}$ as functions of the respective variables. The curves again represent the SM predictions.

Several observations can be made:

- No significant deviations of the measured cross sections from the SM predictions are observed. This is quantified by the χ^2 values which are listed in table 6.

- The differential cross sections $d\sigma/dQ^2$ fall steeply with Q^2 (cf. figure 2), reflecting the influence of the W propagator, the decrease of the parton densities with increasing $x = Q^2/sy$, and the $(1-y)^2$ terms in the cross section. The differences between the e^+p and e^-p cross sections are due to the different x and y behavior (cf. discussion below).

- As can be seen from figure 3, at low x, $d\sigma/dx$ is about the same for e^+p and e^-p scattering. This reflects the fact that the cross sections (equations 1,2) become equal if valence quark distributions can be neglected and if $\overline{d}(x, Q^2) = \overline{u}(x, Q^2)$.

  The decrease of $d\sigma/dx$ with increasing x is more rapid for e^+p scattering than for e^-p scattering. This behavior is also expected from equations 1 and 2: in e^+p reactions, scattering on valence quarks is reduced by the $(1-y)^2$ factor; in addition, the e^+ couples to $d(x, Q^2)$, which is suppressed at high x relative to $u(x, Q^2)$ which is relevant for e^-p scattering (cf. e.g. [38]).

The x dependence of the e^+p to the e^-p cross section ratio is illustrated by the ratios for $x < 0.1$ and for $x > 0.1$ (with $Q^2 > 200$ GeV^2):

$$\frac{\sigma_{e^+p\to\overline{\nu}X}}{\sigma_{e^-p\to\nu X}} = \begin{cases} 0.91\,^{+0.41}_{-0.27}\,[\text{stat}] \pm 0.04\,[\text{syst}] & \text{for} \quad 0 < x < 0.1 \\ \\ 0.26\,^{+0.14}_{-0.09}\,[\text{stat}] \pm 0.01\,[\text{syst}] & \text{for} \quad 0.1 < x < 1\,. \end{cases}$$

The corresponding SM predictions are 0.64 and 0.32. The measured ratios confirm the suppression of the e^+p CC cross section at high x.

The SM predictions for $d\sigma/dx$ have also been evaluated using different parton distribution functions (MRSD$'_-$, GRV, CTEQ 2pM). The largest differences have been observed between the sets MRSD$'_-$ and CTEQ 2pM for x between 0.01 and 0.1, where the cross section predicted by MRSD$'_-$ is up to 10% lower than the CTEQ 2pM values, both for e^+p and e^-p scattering. The MRSA, CTEQ 2pM and GRV predictions agree to better than 5%.

- The measured differential cross sections $d\sigma/dy$ agree with the theoretical predictions. The SM curves in figure 4 reveal that the expected shapes are very similar for e^+p and e^-p scattering, indicating that the relative contributions of the $(1-y)^2$ terms are about equal in both cases.

  As $y \to 1$, the cross section ratio e^+p/e^-p is given by $1/\left(\frac{u_v}{u_s + c} + 1\right)$ (assuming $\overline{u} = u_s$ and $\overline{c} = c$, the indices v and s indicating valence and sea quark distributions, respectively). The fact that the prediction, corresponding to $u_v/(u_s + c) \approx 1$, is above the data for $y > 0.4$, is only moderately significant in view of the large errors.

  At $y \to 0$, the cross section ratio e^+p/e^-p approaches $(d_v + S)/(u_v + S)$, where $S = d_s + u_s + s + c$ (assuming again that the quark and antiquark sea distributions are identical for each flavor).

In order to further study the influence of the $V-A$ helicity structure and the parton distributions, figure 5 shows $d\sigma/dy$ separately for $x < 0.1$ (where sea quarks dominate the cross section) and for $x > 0.1$ (where the valence contribution is larger). Here three equal size y bins are used.

For low x, the predicted y shapes are similar for e^+p and e^-p scattering, the differences being mainly due to residual valence contributions. The most significant deviation of the measured cross sections from the prediction is observed in the lowest y bin ($y < 0.33$), where the measured $\sigma_{e^-p\to\nu X}$ is about two standard deviations below the SM prediction. For $x > 0.1$, both the e^+p and the e^-p cross sections decrease with increasing y. For e^-p, this can be attributed to residual sea quark contributions and to the W propagator which enters via the dependence of the average Q^2 on y. For e^+p scattering, the decrease of $d\sigma/dy$ with increasing y is even faster due to the $(1-y)^2$ term in the cross section. All measured values are compatible with the predictions, indicating that the slight deviations observed at $y \sim 0.3$ in the e^+p/e^-p ratios are due to the low–x data.

Integrated cross sections for $Q^2 > 200\,\mathrm{GeV}^2$

The integrated cross sections for $Q^2 > 200\,\mathrm{GeV}^2$ are obtained by summing the cross sections in the Q^2 bins of tables 2 and 3, resulting in[11]

$$\sigma_{e^+p \to \overline{\nu}X}(Q^2 > 200\,\mathrm{GeV}^2) = 30.3\,{}^{+\ 5.5}_{-\ 4.2}\,[\mathrm{stat}]\,{}^{+1.6}_{-2.6}\,[\mathrm{syst}]\,\mathrm{pb}$$
$$\sigma_{e^-p \to \nu X}(Q^2 > 200\,\mathrm{GeV}^2) = 54.7\,{}^{+15.9}_{-\ 9.8}\,[\mathrm{stat}]\,{}^{+2.8}_{-3.4}\,[\mathrm{syst}]\,\mathrm{pb}\;.$$

These measurements are compatible with the respective SM predictions of $32.3\,\mathrm{pb}$ and $65.8\,\mathrm{pb}$. The e^+p/e^-p ratio is

$$\frac{\sigma_{e^+p \to \overline{\nu}X}}{\sigma_{e^-p \to \nu X}}(Q^2 > 200\,\mathrm{GeV}^2) = 0.55\,{}^{+0.16}_{-0.12}\,[\mathrm{stat}]\,{}^{+0.02}_{-0.03}\,[\mathrm{syst}]\;, \tag{6}$$

in agreement with the SM prediction of 0.49.

Determination of the W mass

The Q^2 dependence of the CC cross section is largely determined by the propagator term $\mathcal{P}(M_W, Q^2) = [M_W^2/(M_W^2 + Q^2)]^2$. In order to determine the value of M_W, the differential cross section was factorized according to $d\sigma/dQ^2 = \mathcal{P}(M_W, Q^2) \cdot \Phi(Q^2)$. The function $\Phi(Q^2)$, containing the Q^2 dependence of the parton densities and couplings, was taken from the MC simulation, using the MRSA parton distributions. A binned log–likelihood fit with M_W as the free parameter, applied simultaneously to the e^+p and e^-p data samples, yielded

$$M_W = 79\,{}^{+8}_{-7}\,[\mathrm{stat}]\,{}^{+4}_{-4}\,[\mathrm{syst}]\,\mathrm{GeV}\;, \tag{7}$$

in agreement with the average value $M_W = 80.22 \pm 0.26\,\mathrm{GeV}$ [39] obtained from direct measurements of the W mass at $p\overline{p}$ colliders [6] and also with the recent H1 measurement [5]. The systematic uncertainty of M_W has been evaluated using the method described in section 4.5. The dominant contribution is the calorimeter energy scale.

5.2   Jet Analysis

An (η, ϕ)–cone jet finding algorithm [40] has been applied to the data, using a cone radius, $R = (\Delta\phi^2 + \Delta\eta^2)^{\frac{1}{2}}$ of 0.7. Pre–clusters are formed around calorimeter cells with transverse energies larger than $0.3\,\mathrm{GeV}$, and the final clusters are called jets if their transverse energies exceed $6\,\mathrm{GeV}$ and their pseudorapidities η^{jet} are less than 2.5 (i.e. polar angles greater than $9°$). This jet analysis is done in the laboratory system. A detailed analysis of jets in NC reactions, covering the region $Q^2 \lesssim 10^3\,\mathrm{GeV}^2$, has previously been published in [41].

The results of the present jet analysis turn out to be insensitive to the choice of the cone radius ($R = 1$ and $R = 0.5$ have also been tested). The constraint on η^{jet} was applied in order to avoid effects from the fragmentation of the proton remnant. In fact, the proton remnant manifests itself as a moderate enhancement of the transverse energy flow around the forward edge of acceptance, and for $\eta^{\mathrm{jet}} = 2.5$ this enhancement is still clearly separated from the E_t flow associated with the jet.

---

[11]Summing the single cross sections implies using an average of the acceptances evaluated for the single bins, which is slightly different from the global acceptance quoted in table 1.

For all jets found, the distributions of the jet momentum transverse to the beam axis, p_t^{jet}, is shown in figures 6a and 7a for e^+p and e^-p data, respectively. p_t^{jet} has been corrected for energy loss in the inactive material of the detector[12] by using the average difference of measured and true values of p_t^{jet} as determined in the MC simulation as a function of the measured p_t^{jet}. Note that the p_t^{jet} spectrum is much harder for the e^-p than for the e^+p data, as is expected from the harder Q^2 distributions. Figures 6b and 7b show the distributions of η^{jet}. The transverse energy flows measured in pseudorapidity ($\Delta\eta$) and azimuthal angle ($\Delta\phi$) relative to the jet axis, are plotted in figures 6c,d and 7c,d. The hadronic energy flow produced between the jet and the proton remnant is clearly observed in the excess of transverse energy at high $\Delta\eta$, i.e. towards the proton remnant.

All these figures also show the predictions of the ARIADNE MC. The p_t^{jet} and η^{jet} distributions are also compared to the MEPS simulation. The MC distributions have been normalized to the number of jets observed in the data. For the E_t flow distributions, the differences between ARIADNE and MEPS (not shown) are slight. Good agreement is observed between the data and both the ARIADNE and the MEPS predictions, indicating in particular that the jet properties are well described by the MC models.

The jet multiplicity distributions are summarized in table 7. All selected events have at least one jet. Events with two or more jets are expected from hard QCD subprocesses, in particular from boson–gluon fusion (BGF). The MC predictions for the jet multiplicities, which include the $\mathcal{O}(\alpha_s)$ matrix elements, exhibit significant differences, amounting to nearly a factor of two in the 2–jet rates. However, within their statistical errors, the data are compatible with both models, favoring values intermediate between ARIADNE and MEPS.

5.3   Search for Large Rapidity Gap Events

Events with a large rapidity gap (LRG) between the outgoing proton system and the rest of the hadronic final state have been observed at HERA in neutral–current DIS [7]. These events are generally understood to be of a diffractive nature and to result from the exchange of a colorless object (usually called the pomeron) with the quantum numbers of the vacuum. Evidence for a partonic structure of the pomeron in DIS has also been observed by the HERA experiments [8].

In CC processes, the coupling of the exchanged W is sensitive to the flavor of the pomeron constituents, which could provide additional information on the pomeron structure. The search also is sensitive to high Q^2 diffractive production of exclusive hadronic states such as vector or axial–vector mesons, complementing corresponding NC studies [42].

Similar to the prescription used in a previous NC analysis [9], LRG events are identified using two variables, $\eta_{\max}$ and θ_H. $\eta_{\max}$ is defined as the maximum pseudorapidity of any calorimeter cluster[13] or cell with energy greater than $400\,\text{MeV}$. The global quantity θ_H is given by the energy weighted mean polar angle of the energy deposits in the calorimeter, $\cos\theta_H = \sum_i p_Z^i / \sum_i E^i$, where the sums run over all calorimeter cells. In the naïve quark parton model, θ_H is the scattering angle of the struck quark.

Figure 8 shows a scatter plot of $\cos\theta_H$ versus $\eta_{\max}$ for the combined e^+p and e^-p samples. The rectangle indicates the region $\eta_{\max}<2.5$ and $\cos\theta_H<0.75$, which is taken from [9] as

---

[12]This was the only correction applied in this jet analysis.

[13]Calorimeter clusters are groups of adjacent cells which have energy deposits above the noise thresholds.

the definition of LRG events ("LRG requirement"). One event of the e^+p sample, shown in figure 9, passes these LRG cuts. The reconstructed kinematic variables for this event are $P_t = 14 \pm 2\,\mathrm{GeV}$, $Q^2 = 300 \pm 70\,\mathrm{GeV}^2$, $x = 0.0093 \pm 0.0015$ and $y = 0.35 \pm 0.10$.

In order to estimate event selection efficiencies and expected event rates in the e^+p case, the LRG analysis was also applied to the following CC MC sets (at the generator level, η_{max} was defined as the maximum pseudorapidity of all particles with momenta greater than $400\,\mathrm{MeV}$ and with $\eta < 4.5$, where the latter requirement excluded the proton in diffractive reactions):

- ARIADNE. This set uses LEPTO for the differential cross section and includes the simulation of diffractive–like processes via soft color interactions between the per-turbatively produced partons and color–charges in the proton remnant [43]. The fraction of events with $\eta_{\mathrm{max}} < 2.5$ at the generator level was found to be 1.3%.

- MEPS. This set also is based on LEPTO, but does not simulate soft color interactions. Here the rapidity gap between proton direction and hadronic system is exponentially suppressed. At the generator level, 0.45% of the events had $\eta_{\mathrm{max}} < 2.5$. Most of the events passing the LRG requirement had a smaller rapidity gap at the generator level.

- POMPYT. This generator simulates only diffractive reactions and is based on a factorizable model for high–energy diffractive processes where, within the PYTHIA framework, the proton emits a pomeron, whose constituents take part in a hard scattering process with the W boson. For this analysis a hard quark density distri-bution in the pomeron was assumed ($\propto \beta(1-\beta)$, where β is the momentum fraction of the quark relative to the pomeron momentum), which in addition satisfied the momentum sum rule.[14]

  It is interesting to note that, according to the POMPYT simulation, only 18% of all CC diffractive events with $Q^2 > 200\,\mathrm{GeV}^2$ have $\eta_{\mathrm{max}} < 2.5$ at the generator level, 41% of which pass the CC selection and fulfill the LRG requirement.

The fractions of LRG events are summarized in table 8 (for the e^+p NC control sample this ratio was determined using the event weights as described in section 3.3). They roughly agree between the CC data, the ARIADNE simulation and the NC control sample, whereas for the MEPS sample, the fraction of LRG events is below that predicted in ARIADNE. The selection efficiency $\varepsilon_{\mathrm{LRG}}$, defined as

$$\varepsilon_{\mathrm{LRG}} = \frac{\text{no. of events with } Q^2_{\mathrm{cor}} > 200\,\mathrm{GeV}^2 \text{ which pass CC cuts and LRG requirement}}{\text{no. of events which have } Q^2 > 200\,\mathrm{GeV}^2 \text{ and } \eta_{\mathrm{max}} < 2.5 \text{ at generator level}},$$

is also shown in table 8 for the three MC sets. Using the ARIADNE value of $\varepsilon_{\mathrm{LRG}} = 0.43$, the cross section for e^+p CC interactions with $\eta_{\mathrm{max}} < 2.5$ was calculated to be

$$\sigma_{e^+p \to \bar{\nu}X}(Q^2 > 200\,\mathrm{GeV}^2; \eta_{\mathrm{max}} < 2.5) = 0.8\,^{+1.8}_{-0.7}\,[\text{stat}] \pm 0.1\,[\text{syst}]\,\mathrm{pb}. \tag{8}$$

The systematic uncertainty of this result was derived from the difference of the efficiencies $\varepsilon_{\mathrm{LRG}}$ obtained using the MEPS and POMPYT sets.

---

[14]The latter assumption conflicts with measurements [9] of the NC diffractive cross section. Hence POMPYT predictions of absolute cross sections were not used.

6 Summary and Conclusions

The cross sections for the deep inelastic charged–current interactions $e^+p \to \overline{\nu}X$ and $e^-p \to \nu X$ have been measured in the kinematic region $x > 0.006$ and $Q^2 > 200\,\mathrm{GeV}^2$, using the e^+p and e^-p data collected with the ZEUS detector during 1993 and 1994. For the integrated cross sections,

$$\sigma_{e^+p \to \overline{\nu}X}(Q^2 > 200\,\mathrm{GeV}^2) = 30.3\,^{+\,5.5}_{-\,4.2}\,[\mathrm{stat}]\,^{+1.6}_{-2.6}\,[\mathrm{syst}]\,\mathrm{pb}$$
$$\sigma_{e^-p \to \nu X}(Q^2 > 200\,\mathrm{GeV}^2) = 54.7\,^{+15.9}_{-\,9.8}\,[\mathrm{stat}]\,^{+2.8}_{-3.4}\,[\mathrm{syst}]\,\mathrm{pb}$$

are obtained, in good agreement with the Standard Model expectations of $32.3\,\mathrm{pb}$ and $65.8\,\mathrm{pb}$.

The differential cross sections have been measured as functions of Q^2, x and y. The differences between e^+p and e^-p scattering, which are expected from the $V-A$ helicity structure of the weak interaction and from the quark content of the proton, are clearly observed. No significant deviation from the Standard Model predictions is found.

The measured Q^2 dependence of the differential cross sections for e^+ and e^- induced CC DIS reactions is used to determine the W mass. The measured value of M_W is $79\,^{+8}_{-7}\,^{+4}_{-4}\,\mathrm{GeV}$, in good agreement with direct measurements performed at $p\overline{p}$ colliders.

A jet analysis has been performed and CC events with multiple jets have been observed. The distributions of the jet transverse momentum and rapidity as well as transverse energy flow jet profiles have been measured and are compared to the $\mathcal{O}(\alpha_s)$ predictions of the ARIADNE and MEPS Monte Carlo models. Good agreement is observed in both the jet profiles and the jet rates.

A search for charged–current events with a large rapidity gap between the observed hadronic system and the outgoing proton system yielded one candidate event in the e^+p sample, corresponding to a cross section of $\sigma_{e^+p \to \overline{\nu}X}(Q^2 > 200\,\mathrm{GeV}^2; \eta_{\mathrm{max}} < 2.5) = 0.8\,^{+1.8}_{-0.7}\,[\mathrm{stat}]\,\pm 0.1\,[\mathrm{syst}]\,\mathrm{pb}$.

Acknowledgments

References

[1] CDHS Collaboration, H.Abramowicz et al., Z. Phys. **C25**(1984)29;
    CDHSW Collaboration, J.P.Berge et al., Z. Phys. **C49**(1991)187;
    CCFR Collaboration, E.Oltman et al., Z. Phys. **C53**(1992)51;
    BEBC WA21 Collaboration, G.T.Jones et al., Z. Phys. **C62**(1994)575.

[2] H1 Collaboration, T.Ahmed et al., Phys. Lett. **B324**(1994)241.

[3] ZEUS Collaboration, M.Derrick et al., Phys. Rev. Lett. **75**(1995)1006.

[4] H1 Collaboration, S.Aid et al., Z. Phys. **C67**(1995)565.

[5] H1 Collaboration, S.Aid et al., DESY 96–046 (1996).

[6] CDF Collaboration, F.Abe et al., Phys. Rev. Lett. **75**(1995)11;
    CDF Collaboration, F.Abe et al., Phys. Rev. **D52**(1995)4784;
    D0 Collaboration, S.Abachi et al., Proc. Topical Workshop on Proton–Antiproton
    Collider Physics, Tsukuba, Japan (1993);
    UA2 Collaboration, J.Alitti et al., Phys. Lett **B241**(1990)150.

[7] ZEUS Collaboration, M.Derrick et al., Phys. Lett. **B315**(1993)481;
    ZEUS Collaboration, M.Derrick et al., Phys. Lett. **B332**(1994)228;
    H1 Collaboration, T.Ahmed et al., Nucl. Phys. **B429**(1994)477.

[8] ZEUS Collaboration, M.Derrick et al., Phys. Lett. **B346**(1995)399;
    H1 Collaboration, T.Ahmed et al., Phys. Lett. **B348**(1995)681;
    ZEUS Collaboration, M.Derrick et al., Phys. Lett. **B356**(1995)129.

[9] ZEUS Collaboration, M.Derrick et al., Z. Phys. **C68**(1995)569.

[10] ZEUS Collaboration, M.Derrick et al., DESY 96–018 (1996).

[11] ZEUS Collaboration, M.Derrick et al., Z. Phys. **C65**(1995)379.

[12] ZEUS Collaboration, M.Derrick et al., Phys. Lett. **B293**(1992)465.

[13] The ZEUS Detector, Status Report 1993, DESY (1993).

[14] M.Derrick et al., Nucl. Inst. Meth. **A309**(1991)77;
    A.Andresen et al., Nucl. Inst. Meth. **A309**(1991)101;
    A.Bernstein et al., Nucl. Inst. Meth. **A336**(1993)23;
    A.Caldwell et al., Nucl. Inst. Meth. **A321**(1992)356.

[15] H.Abramowicz et al., Nucl. Inst. Meth. **A313**(1992)126.

[16] C.Alvisi et al., Nucl. Inst. Meth. **A305**(1991)30.

[17] N.Harnew et al., Nucl. Inst. Meth. **A279**(1989)290;
    B.Foster et al., Nucl. Phys., Proc. Suppl. **B32**(1993);
    B.Foster et al., Nucl. Inst. Meth. **A338**(1994)254.

[18] J.Andruszków, DESY 92–066 (1992).

[19] LEPTO 6.3: G.Ingelman, Proc. 1991 Workshop on Physics at HERA, ed. W.Buchmüller and G.Ingelman (DESY, Hamburg, 1992), Vol. 3, p.1366.

[20] HERACLES 4.4: A.Kwiatkowski, H.Spiesberger and H.J.Möhring, Proc. 1991 Workshop on Physics at HERA, ed. W.Buchmüller and G.Ingelman (DESY, Hamburg, 1992), Vol. 3, p.1294.

[21] DJANGO 6.1: G.Schuler and H.Spiesberger, Proc. 1991 Workshop on Physics at HERA, ed. W.Buchmüller and G.Ingelman (DESY, Hamburg, 1992), Vol. 3, p.1419.

[22] A.D.Martin, R.G.Roberts, W.J.Stirling, Phys. Rev. **D50**(1994)6734.

[23] ARIADNE 4.06: L.Lönnblad, LU TP–89–10;
L.Lönnblad, Comp. Phys. Comm. **71**(1992)15.

[24] PYTHIA 5.7 and JETSET 7.4: T.Sjöstrand, CERN–TH 7112–93 (1994);
T.Sjöstrand, LU–TP–95–20 (1995).

[25] HERWIG 5.8: B.R.Webber, Proc. 1991 Workshop on Physics at HERA, ed. W.Buchmüller and G.Ingelman (DESY, Hamburg, 1992), Vol. 3, p.1363.

[26] AROMA 2.1: G.Ingelman and G.Schuler, Proc. 1991 Workshop on Physics at HERA, ed. W.Buchmüller and G.Ingelman (DESY, Hamburg, 1992), Vol. 3, p.1346.

[27] POMPYT 1.0: P.Bruni and G.Ingelman, Proc. Europhysics Conference on HEP, Marseilles, France (1993), p.595.

[28] G.Ingelman and P.Schlein, Phys. Lett. **B152**(1985)256.

[29] R.Brun et al., CERN DD/EE–84–1 (1987).

[30] F.Jacquet and A.Blondel, Proceedings of the study for an *ep* facility for Europe, DESY 79–48 (1979), p.391.

[31] H.Abramowicz, A.Caldwell, R.Sinkus, Nucl. Inst. Meth. **A365**(1995)508.

[32] S.Bentvelsen, J.Engelen, P.Kooijman, Proc. 1991 Workshop on Physics at HERA, ed. W.Buchmüller and G.Ingelman (DESY, Hamburg, 1992), Vol. 1, p.23.

[33] G.D'Agostini, DESY 94–099 (1994).

[34] A.D.Martin, R.G.Roberts, W.J.Stirling, Phys. Rev. **D47**(1993)867.

[35] A.D.Martin, R.G.Roberts, W.J.Stirling, Phys. Lett. **306B**(1993)147;
erratum in Phys. Lett. **309B**(1993)492.

[36] M.Glück, E.Reya, A.Vogt, Z. Phys. **C53**(1992)127.

[37] CTEQ Collaboration, J.Botts et al., Phys. Lett. **B304**(1993)159.

[38] BEBC WA21 Collaboration, G.T.Jones et al., Z. Phys. **C62**(1994)601.

[39] L.Montanet et al., Phys. Rev. **D50**(1994)1173.

[40] UA1 Collaboration, G.Arnison et al., Phys. Lett. **B123**(1983)115;
      J.Huth et al., Proc. 1990 DPF Summer Study on High–Energy Physics, Snowmass,
      Colorado, ed. E.L.Berger (World Scientific, Singapore, 1990, p.134).

[41] ZEUS Collaboration, M.Derrick et al., Z. Phys. **C67**(1995)81.

[42] ZEUS Collaboration, M.Derrick et al., Phys. Lett. **B356**(1995)601;
      H1 Collaboration, S.Aid et al., DESY 96–023.

[43] A.Edin, G.Ingelman, J.Rathsman, DESY 95-145 (1995).

cut	e^+p		e^-p	
description	data	MC($Q^2{>}200\,\mathrm{GeV}^2$)	data	MC($Q^2{>}200\,\mathrm{GeV}^2$)
$Q^2 > 200\,\mathrm{GeV}^2$ (MC only)	—	100 %	—	100 %
Trigger and preselection	6307	83.2%	1450	86.1%
$\not{P}_t > 11\,\mathrm{GeV}$	2981	80.0%	940	83.1%
$|Z_\mathrm{vtx}| < 45\,\mathrm{cm}$	1283	71.0%	500	74.7%
$\not{P}_t^{\,\mathrm{out}}/\not{P}_t > 0.6$	958	70.3%	301	73.9%
good track	741	68.2%	237	71.7%
$|\Delta\phi| < 1$	342	66.8%	113	70.3%
$y_{JB} < 0.8$	279	66.2%	98	69.2%
$\not{P}_t/E_t > 0.4$	208	65.0%	59	68.1%
$P_t^{\mathrm{tracks}}/\not{P}_t > 0.1$	87	63.0%	36	66.3%
Muon,timing,sparks	59	63.0%	30	66.3%
Visual scan (data only)	56	—	30	—

Table 1: Data reduction by the selection cuts described in section 3.2. The columns denoted "data" indicate the numbers of events remaining after applying the cuts. The "MC" columns show the cumulative selection efficiencies for the ARIADNE MC simulation.

e^+p	Q^2 [GeV^2]					
	200 – 437	437 – 955	955 – 2089	2089 – 4517	4517 – 10000	> 200
N_{evt}	8	15	12	14	7	56
$\langle Q^2 \rangle$ [GeV^2]	310	670	1450	3070	6510	1910
N_{bg}	1.2	0.2	0	0	0	1.4
ζ	0.38	0.58	0.70	0.76	0.71	0.62
ξ	0.76	0.72	0.73	0.76	0.79	1.0
σ^{exp} [pb]	6.1	8.7	5.8	6.3	3.4	30.3
$\Delta\sigma^{\text{exp}}$ [stat] [pb]	+ 3.0 − 2.2	+ 2.9 − 2.3	+ 2.2 − 1.7	+ 2.2 − 1.7	+ 1.8 − 1.3	+ 5.5 − 4.2
$\Delta\sigma^{\text{exp}}$ [syst] [pb]	+ 1.3 − 2.7	+ 0.6 − 0.6	+ 0.3 − 0.3	+ 0.6 − 0.3	+ 0.7 − 0.4	+ 1.6 − 2.6
σ^{th} [pb]	6.2	8.3	8.3	6.4	2.5	32.3
Systematic checks						
Check	$\Delta\sigma^{\text{exp}}$ [%]					
E scale $+3\%$ ($+5\%$ in FCAL)	12.6	6.3	2.1	− 3.3	−10.8	2.1
E scale -3% (-5% in FCAL)	−18.7	− 3.0	− 3.3	3.8	13.6	− 2.0
Unfolding	− 0.9	1.1	1.7	− 1.5	13.8	− 1.0
Q^2, x, y reconstruction	−15.7	− 2.1	2.0	7.6	5.8	− 0.3
$N_{\text{bg}} + \Delta N_{\text{bg}}$	−36.2	− 3.4	0.0	0.0	0.0	− 7.3
$N_{\text{bg}} - \Delta N_{\text{bg}}$	16.1	1.5	0.0	0.0	0.0	3.3

Table 2: Cross sections for CC e^+p scattering in intervals of Q^2, and for $Q^2 > 200\,\text{GeV}^2$. The rows denoted N_{evt}, $\langle Q^2 \rangle$, N_{bg}, ζ, ξ, σ^{exp}, and σ^{th} show the raw event numbers, the mean Q^2 according to the SM prediction, the estimated number of background events from photoproduction, the bin–by–bin acceptance corrections, the purities, the experimental cross sections, and the theoretical cross sections, respectively. For σ^{exp} the statistical errors $\Delta\sigma^{\text{exp}}$ [stat] and systematic uncertainties $\Delta\sigma^{\text{exp}}$ [syst] are quoted. The latter are calculated from the deviations resulting from the systematic studies described in the text (including the luminosity uncertainty of 3% and the overall uncertainty of 3% assigned to the efficiency of those selection cuts involving track quantities). The dominant contributions are detailed in the lower part of the table.

e^-p	Q^2 [GeV^2]						
	200 – 437	437 – 955	955 – 2089	2089 – 4517	4517 – 10000	10000 – 21877	> 200
N_{evt}	3	3	7	6	9	2	30
$\langle Q^2 \rangle$ [GeV^2]	310	670	1470	3140	6700	13900	3340
N_{bg}	0.3	0.1	0	0	0	0	0.4
ζ	0.39	0.56	0.74	0.78	0.74	0.59	0.66
ξ	0.74	0.73	0.70	0.74	0.80	0.83	1.0
σ^{exp} [pb]	8.4	6.3	11.6	9.4	14.9	4.1	54.7
$\Delta\sigma^{\text{exp}}$ [stat] [pb]	+ 8.2 − 4.6	+ 6.2 − 3.4	+ 6.3 − 4.3	+ 5.6 − 3.7	+ 6.8 − 4.9	+ 5.4 − 2.7	+15.9 − 9.8
$\Delta\sigma^{\text{exp}}$ [syst] [pb]	+ 1.6 − 2.7	+ 0.6 − 0.7	+ 0.7 − 0.7	+ 0.8 − 0.6	+ 1.9 − 1.6	+ 1.5 − 1.2	+ 2.8 − 2.9
σ^{th} [pb]	7.9	12.2	15.1	15.7	10.6	3.7	65.8
Systematic checks							
Check	$\Delta\sigma^{\text{exp}}$ [%]						
E scale +3% (+5% in FCAL)	14.2	7.1	2.8	0.9	− 3.9	−24.9	2.0
E scale −3% (−5% in FCAL)	−10.9	− 7.8	− 2.6	1.2	9.5	26.9	1.1
Unfolding	− 0.5	0.0	− 3.3	− 4.2	− 9.3	24.3	− 2.1
Q^2, x, y reconstruction	−15.2	− 5.9	2.2	6.8	7.8	−14.5	− 1.0
$N_{\text{bg}} + \Delta N_{\text{bg}}$	−25.9	− 5.0	0.0	0.0	0.0	0.0	− 4.0
$N_{\text{bg}} - \Delta N_{\text{bg}}$	11.1	2.7	0.0	0.0	0.0	0.0	1.7

Table 3: Cross sections for CC e^-p scattering in intervals of Q^2, and for $Q^2 > 200\,\text{GeV}^2$. The rows denoted N_{evt}, $\langle Q^2 \rangle$, N_{bg}, ζ, ξ, σ^{exp}, and σ^{th} show the raw event numbers, the mean Q^2 according to the SM prediction, the estimated number of background events from photoproduction, the bin–by–bin acceptance corrections, the purities, the experimental cross sections, and the theoretical cross sections, respectively. For σ^{exp} the statistical errors $\Delta\sigma^{\text{exp}}$ [stat] and systematic uncertainties $\Delta\sigma^{\text{exp}}$ [syst] are quoted. The latter are calculated from the deviations resulting from the systematic studies described in the text (including the luminosity uncertainty of 2% and the overall uncertainty of 3% assigned to the efficiency of those selection cuts involving track quantities). The dominant contributions are detailed in the lower part of the table.

e^+p	x					
	0.006 – 0.014	0.014 – 0.033	0.033 – 0.076	0.076 – 0.17	0.17 – 0.40	0.40 – 1.0
N_{evt}	3	20	11	13	9	0
$\langle x \rangle$	0.010	0.023	0.052	0.115	0.249	0.480
N_{bg}	1.4	0	0	0	0	0
ζ	0.41	0.78	0.79	0.68	0.48	0.18
ξ	0.68	0.72	0.77	0.82	0.88	0.84
σ^{exp} [pb]	1.3	8.7	4.7	6.5	6.4	0.0
$\Delta\sigma^{\text{exp}}$ [stat] [pb]	$+\,1.3$ $-\,0.7$	$+\,2.4$ $-\,1.9$	$+\,1.9$ $-\,1.4$	$+\,2.3$ $-\,1.8$	$+\,2.9$ $-\,2.1$	$+\,3.5$ $-\,0.0$
$\Delta\sigma^{\text{exp}}$ [syst] [pb]	$+\,1.0$ $-\,1.3$	$+\,0.5$ $-\,0.7$	$+\,0.4$ $-\,0.2$	$+\,0.5$ $-\,0.7$	$+\,0.8$ $-\,0.6$	$+\,0.0$ $-\,0.0$
σ^{th} [pb]	3.4	6.3	8.4	8.3	4.2	0.5

e^-p	x					
	0.006 – 0.014	0.014 – 0.033	0.033 – 0.076	0.076 – 0.17	0.17 – 0.40	0.40 – 1.0
N_{evt}	3	5	5	9	8	0
$\langle x \rangle$	0.010	0.024	0.053	0.119	0.256	0.489
N_{bg}	0.4	0	0	0	0	0
ζ	0.41	0.77	0.84	0.72	0.55	0.17
ξ	0.61	0.73	0.73	0.85	0.87	0.83
σ^{exp} [pb]	7.8	7.9	7.3	15.3	17.6	0.0
$\Delta\sigma^{\text{exp}}$ [stat] [pb]	$+\,7.6$ $-\,4.2$	$+\,5.3$ $-\,3.4$	$+\,4.9$ $-\,3.2$	$+\,7.0$ $-\,5.1$	$+\,8.7$ $-\,6.3$	$+13.2$ $-\,0.0$
$\Delta\sigma^{\text{exp}}$ [syst] [pb]	$+\,1.5$ $-\,2.5$	$+\,0.7$ $-\,0.7$	$+\,0.4$ $-\,0.5$	$+\,1.1$ $-\,2.0$	$+\,3.0$ $-\,1.6$	$+\,0.0$ $-\,0.0$
σ^{th} [pb]	4.2	8.4	14.9	19.2	14.8	2.7

Table 4: Cross sections for CC e^+p (top) and e^-p (bottom) scattering for $Q^2 > 200\,\text{GeV}^2$ in intervals of x. The rows denoted N_{evt}, $\langle x \rangle$, N_{bg}, ζ, ξ, σ^{exp}, and σ^{th} show the raw event numbers, the mean x according to the SM prediction, the estimated number of background events from photoproduction, the bin–by–bin acceptance corrections, the purities, the experimental cross sections, and the theoretical cross sections, respectively. For σ^{exp} the statistical errors $\Delta\sigma^{\text{exp}}$ [stat] and systematic uncertainties $\Delta\sigma^{\text{exp}}$ [syst] are quoted.

e^+p	y				
	0.0 – 0.2	0.2 – 0.4	0.4 – 0.6	0.6 – 0.8	0.8 – 1.0
N_{evt}	14	27	11	3	1
$\langle y \rangle$	0.101	0.293	0.496	0.695	0.895
N_{bg}	0	0.2	1.2	0	0
ζ	0.49	0.86	0.79	0.73	0.15
ξ	0.90	0.79	0.77	0.70	0.80
σ^{exp} [pb]	9.6	10.7	4.2	1.4	2.3
$\Delta\sigma^{\mathrm{exp}}$ [stat] [pb]	+ 3.3 − 2.5	+ 2.5 − 2.1	+ 1.7 − 1.3	+ 1.4 − 0.8	+ 5.4 − 1.9
$\Delta\sigma^{\mathrm{exp}}$ [syst] [pb]	+ 0.5 − 0.7	+ 0.6 − 0.5	+ 0.6 − 1.0	+ 0.2 − 0.1	+ 0.6 − 1.1
σ^{th} [pb]	11.8	8.3	5.4	3.7	3.0

e^-p	y				
	0.0 – 0.2	0.2 – 0.4	0.4 – 0.6	0.6 – 0.8	0.8 – 1.0
N_{evt}	6	5	11	5	3
$\langle y \rangle$	0.101	0.293	0.496	0.696	0.895
N_{bg}	0	0.1	0.3	0	0
ζ	0.51	0.91	0.81	0.77	0.20
ξ	0.92	0.79	0.81	0.74	0.90
σ^{exp} [pb]	14.4	6.6	16.2	7.9	19.0
$\Delta\sigma^{\mathrm{exp}}$ [stat] [pb]	+ 8.6 − 5.7	+ 4.4 − 2.9	+ 6.4 − 4.9	+ 5.2 − 3.4	+18.5 −10.3
$\Delta\sigma^{\mathrm{exp}}$ [syst] [pb]	+ 1.2 − 1.6	+ 0.3 − 0.4	+ 1.3 − 1.4	+ 0.8 − 0.5	+ 4.4 − 7.6
σ^{th} [pb]	23.7	15.6	11.0	8.7	6.9

Table 5: Cross sections for CC e^+p (top) and e^-p (bottom) scattering for $Q^2 > 200\,\mathrm{GeV}^2$ in intervals of y. The rows denoted N_{evt}, $\langle y \rangle$, N_{bg}, ζ, ξ, σ^{exp}, and σ^{th} show the raw event numbers, the mean y according to the SM prediction, the estimated number of background events from photoproduction, the bin–by–bin acceptance corrections, the purities, the experimental cross sections, and the theoretical cross sections, respectively. For σ^{exp} the statistical errors $\Delta\sigma^{\mathrm{exp}}$ [stat] and systematic uncertainties $\Delta\sigma^{\mathrm{exp}}$ [syst] are quoted.

Distribution	χ^2	N_{DOF}	$p(\chi^2, N_{\mathrm{DOF}})$
$d\sigma/d\,Q^2\ (e^+p)$	1.9	5	0.86
$d\sigma/d\,Q^2\ (e^-p)$	3.2	6	0.78
$d\sigma/d\,x\ (e^+p)$	9.9	5	0.08
$d\sigma/d\,x\ (e^-p)$	3.7	5	0.59
$d\sigma/d\,y\ (e^+p)$	5.0	5	0.42
$d\sigma/d\,y\ (e^-p)$	7.8	5	0.17

Table 6: Quality of agreement between experimental results and SM predictions: for the various differential cross sections χ^2, N_{DOF}, and $p(\chi^2, N_{\mathrm{DOF}})$ denote the χ^2 value calculated using statistical errors only, the number of degrees of freedom, and the corresponding χ^2–probability.

N_{jets}	e^+p				e^-p			
	N_{evt}	$R_{\text{jet}}^{\text{data}}$ [%]	$R_{\text{jet}}^{\text{MC}}$ [%]		N_{evt}	$R_{\text{jet}}^{\text{data}}$ [%]	$R_{\text{jet}}^{\text{MC}}$ [%]	
			ARIA.	MEPS			ARIA.	MEPS
0	0	$0.0\,^{+3.2}_{-0.0}$	0.4 ± 0.1	0.4 ± 0.1	0	$0.0\,^{+6.0}_{-0.0}$	0.3 ± 0.1	0.4 ± 0.1
1	49	$87.5\,^{+4.5}_{-6.1}$	90.9 ± 0.4	82.2 ± 0.6	27	$90.0\,^{+5.4}_{-8.8}$	91.6 ± 0.4	83.3 ± 0.5
2	6	$10.7\,^{+5.9}_{-4.2}$	8.4 ± 0.4	16.3 ± 0.5	3	$10.0\,^{+8.8}_{-5.4}$	7.8 ± 0.4	14.6 ± 0.5
3	1	$1.8\,^{+4.0}_{-1.5}$	0.3 ± 0.1	1.1 ± 0.2	0	$0.0\,^{+6.0}_{-0.0}$	0.3 ± 0.1	1.2 ± 0.2

Table 7: Jet rates for e^+p and e^-p data. The columns denoted N_{evt} show the numbers of events in the CC samples which have N_{jets} jets in addition to the proton remnant (for the jet definition see text). The $R_{\text{jet}}^{\text{data}}$ are the corresponding jet rates, which are also given for the ARIADNE and MEPS MC simulations ($R_{\text{jet}}^{\text{MC}}$). Only statistical errors are shown.

data set	R_{LRG} [%]	ε_{LRG} [%]
CC e^+p	$1.8\,^{+\,4.0}_{-\,1.5}$	—
ARIADNE e^+p	$0.9\,^{+\,0.2}_{-\,0.1}$	43
MEPS e^+p	0.3 ± 0.1	39
POMPYT e^+p	13.8 ± 0.5	53
NC control sample (e^+p)	0.9 ± 0.4	—

Table 8: The fraction of large rapidity gap (LRG) events in the e^+p CC sample, in the ARIADNE, MEPS and POMPYT CC MC sets, and in the NC control sample. R_{LRG} denotes the fraction of events with $\eta_{\text{max}} < 2.5$ and $\cos\theta_H < 0.75$ (LRG events) in the total samples passing the CC selection cuts. For the NC control sample, R_{LRG} is calculated from the sums of cross–section weights as described in section 3.3. The selection efficiency ε_{LRG} is defined as the ratio of the number of events which pass the CC cuts, fulfil the LRG requirement and have $Q_{\text{cor}}^2 > 200\,\text{GeV}^2$ to the number of events having $\eta_{\text{max}} < 2.5$ and $Q^2 > 200\,\text{GeV}^2$ at the generator level.
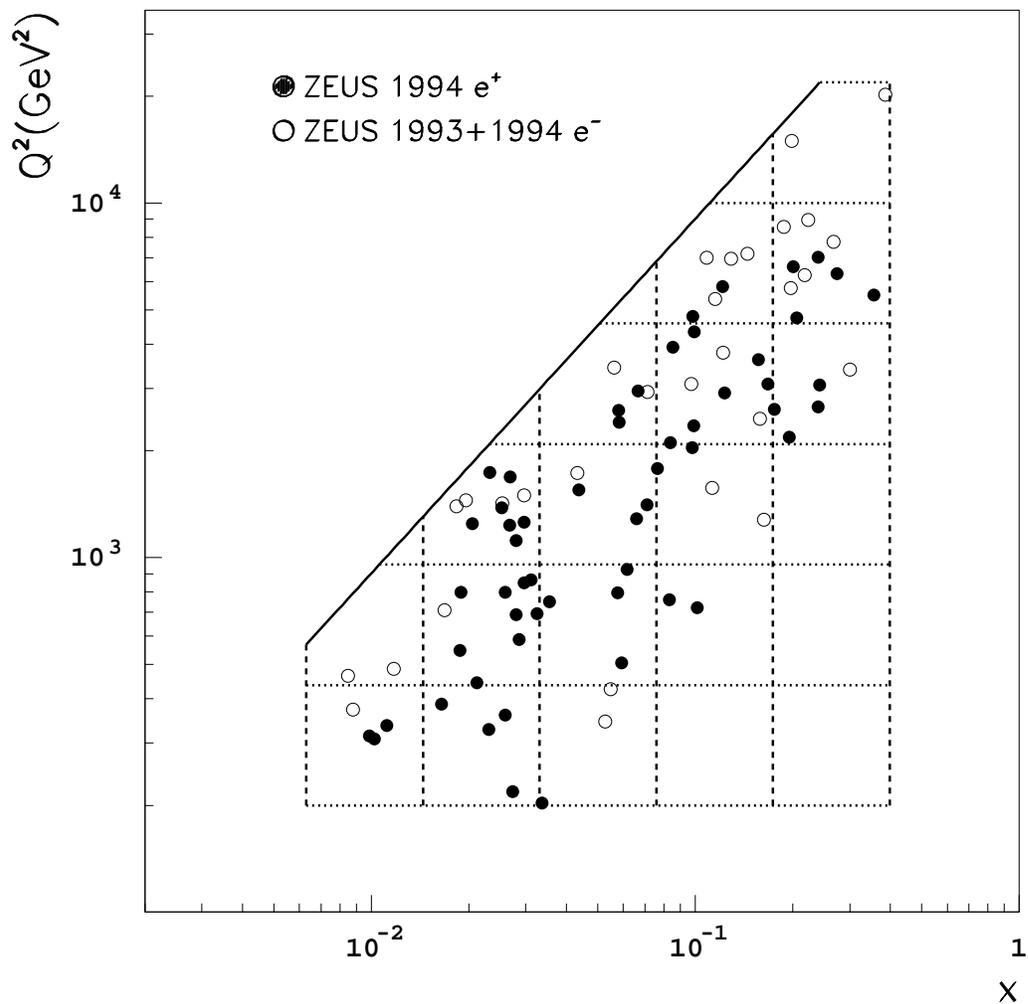
ZEUS 1993+1994

Figure 1: Distribution of events in the (x, Q^2) plane. The filled (open) circles indicate the selected e^+p (e^-p) CC events in a sample with integrated luminosity of $2.93\,\mathrm{pb}^{-1}$ $(0.82\,\mathrm{pb}^{-1})$. The horizontal lines of the grid show the Q^2, the vertical lines the x bins used for the analysis. The solid diagonal line indicates the kinematic limit $y = 1$.
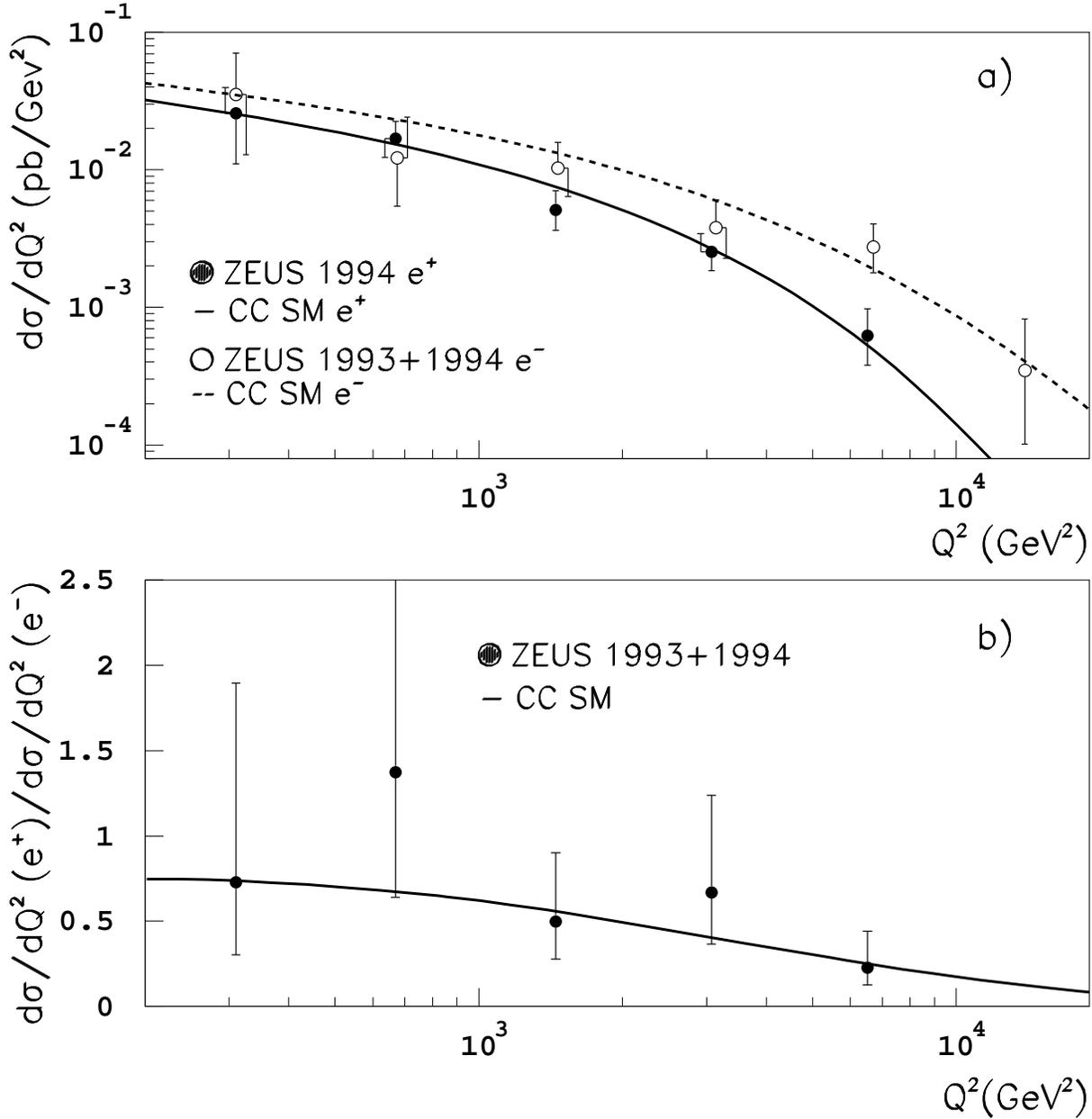
ZEUS 1993+1994

Figure 2: Differential CC cross section versus Q^2. In a), the filled (open) dots and the solid (dashed) curve represent the measured values and the Standard Model (SM) prediction of $d\sigma/dQ^2$ for e^+p (e^-p) collisions. Plot b) shows $(d\sigma_{e^+p\to\bar{\nu}X}/dQ^2)/(d\sigma_{e^-p\to\nu X}/dQ^2)$. The error bars indicate the statistical and systematic uncertainties combined in quadrature. The horizontal position of the points is given by the generator level Q^2 average of the MC events in each bin.
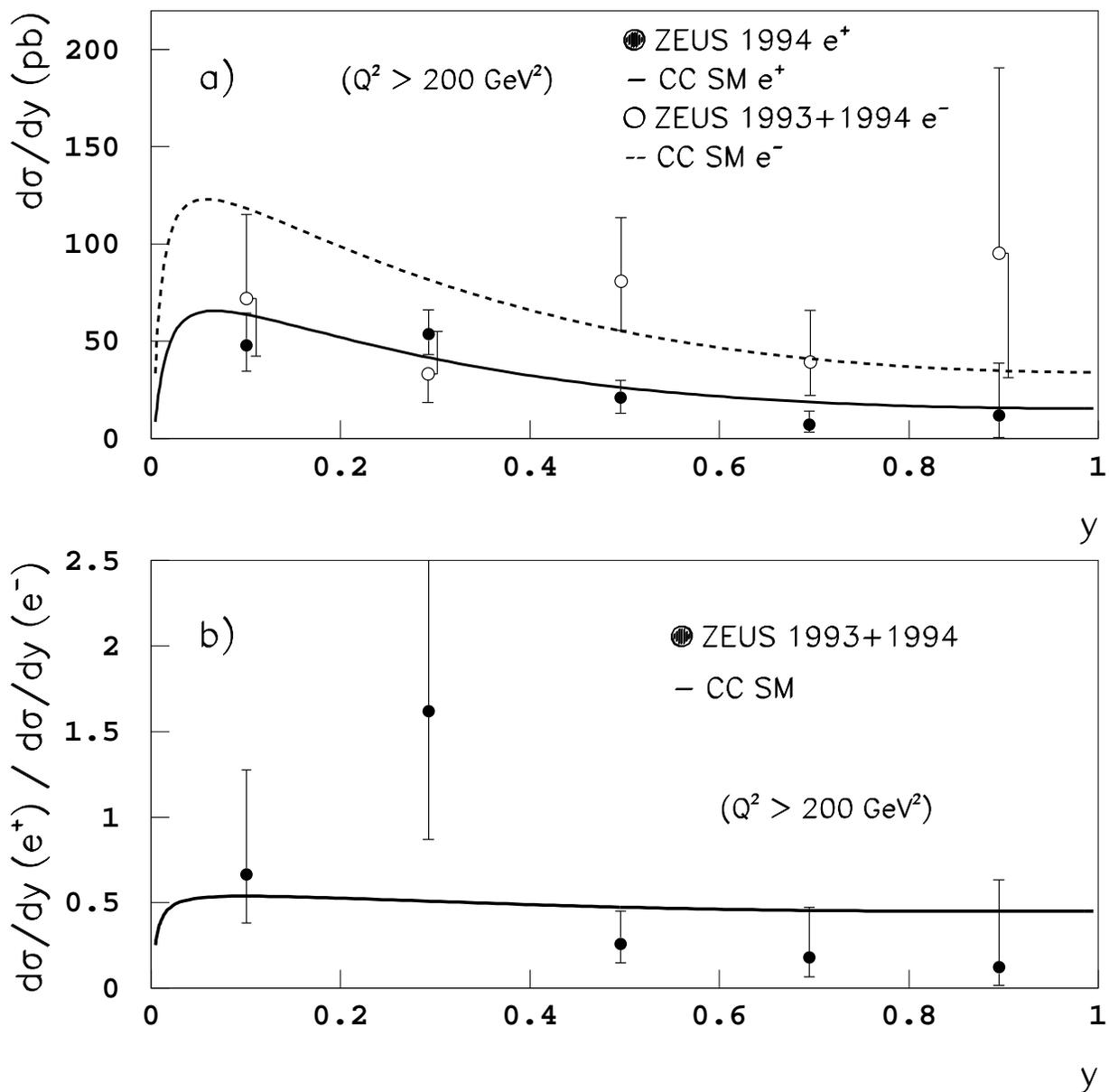
ZEUS 1993+1994
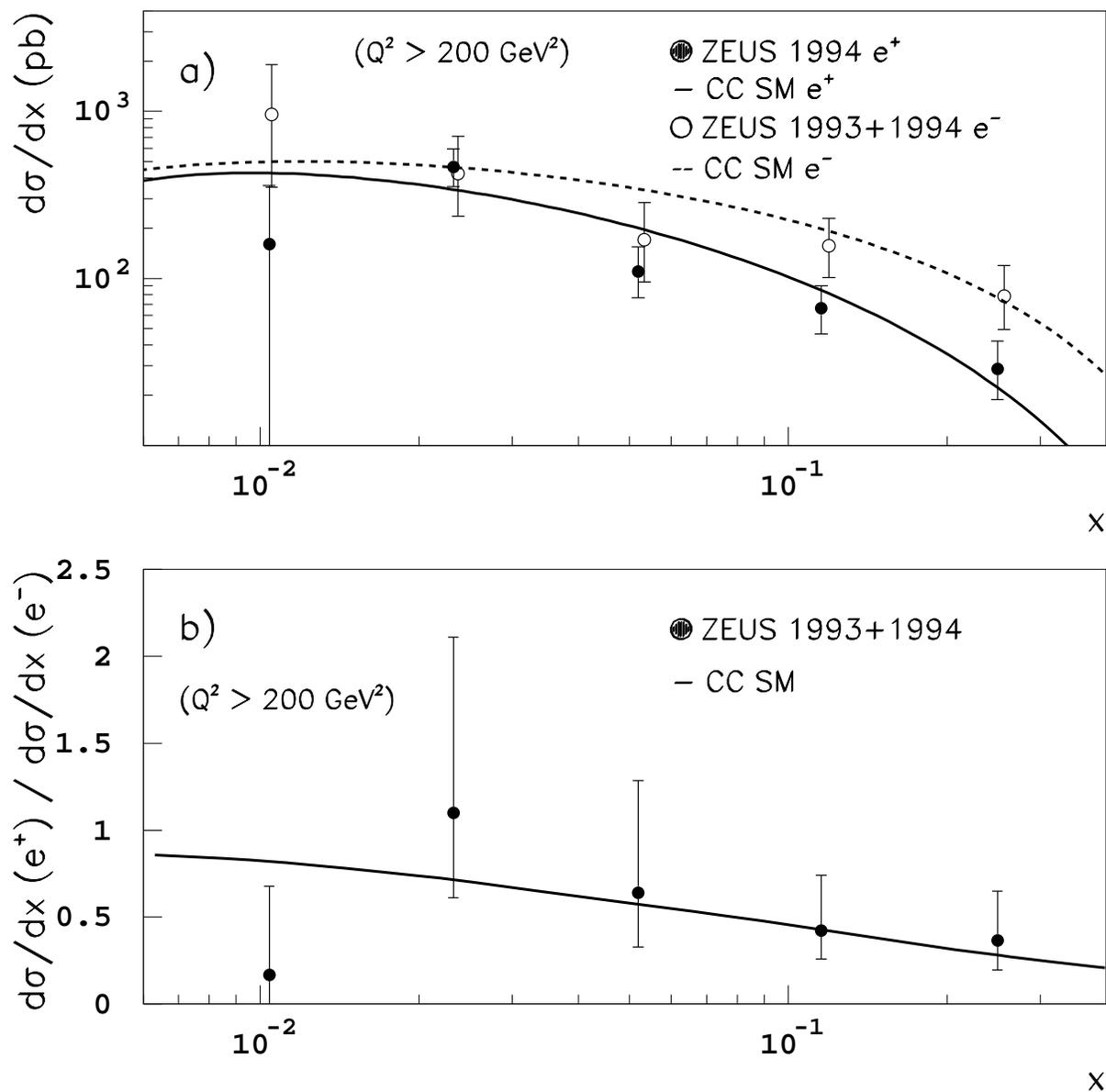
Figure 3: Differential CC cross section versus x for $Q^2 > 200\,\mathrm{GeV}^2$. In a), the filled (open) dots and the solid (dashed) curve represent the measured values and the Standard Model (SM) prediction of $d\sigma/d\,x$ for e^+p (e^-p) collisions. Plot b) shows $(d\sigma_{e^+p\to\overline{\nu}X}/d\,x)/(d\sigma_{e^-p\to\nu X}/d\,x)$. The error bars indicate the statistical and systematic uncertainties combined in quadrature. The horizontal position of the points is given by the generator level x average of the MC events in each bin.
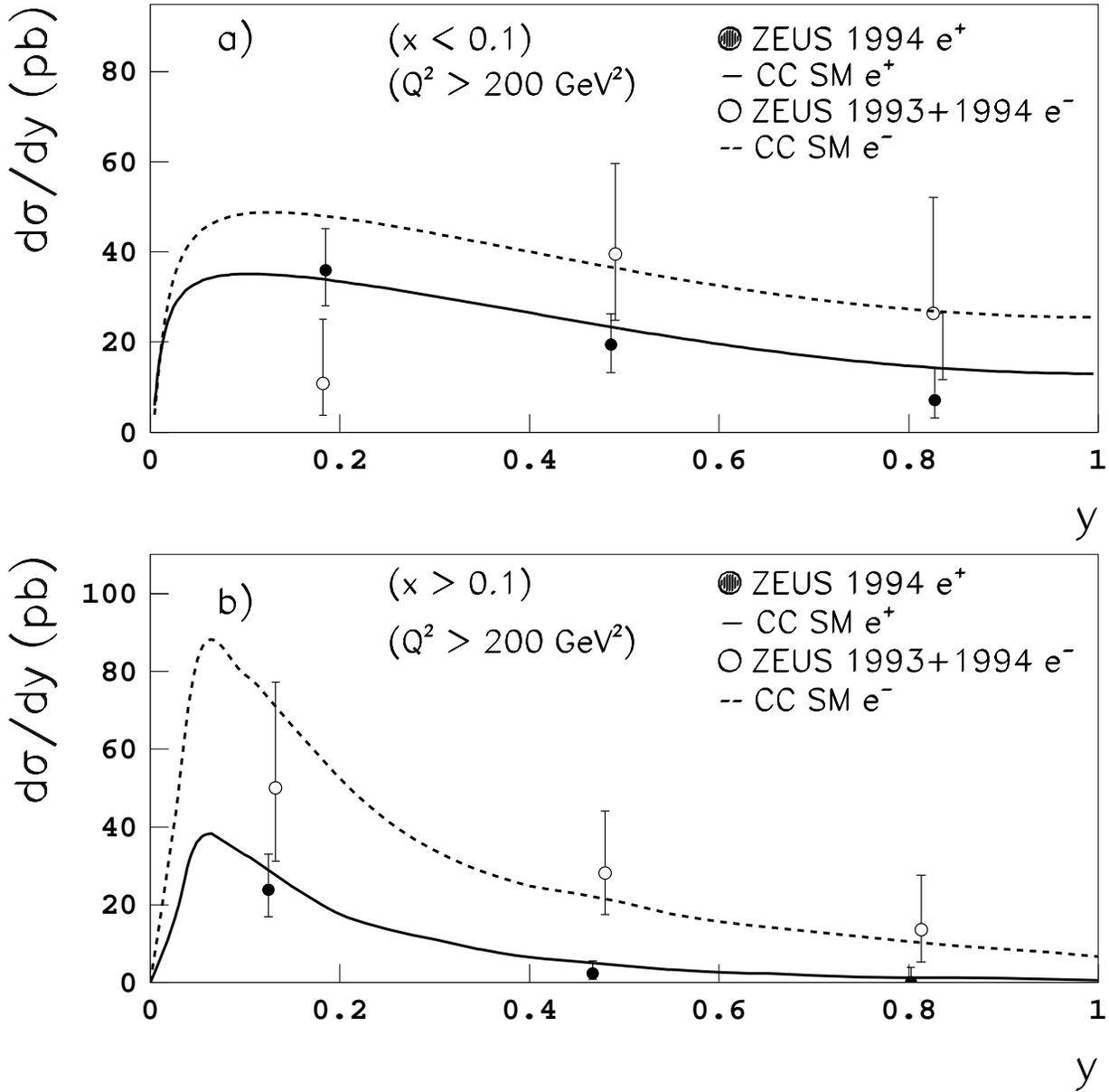
ZEUS 1993+1994

Figure 4: Differential CC cross section versus y for $Q^2 > 200\,\mathrm{GeV}^2$. In a), the filled (open) dots and the solid (dashed) curve represent the measured values and the Standard Model (SM) prediction of $d\sigma/dy$ for e^+p (e^-p) collisions. Plot b) shows $(d\sigma_{e^+p\to\bar{\nu}X}/dy)/(d\sigma_{e^-p\to\nu X}/dy)$. The error bars indicate the statistical and systematic uncertainties combined in quadrature. The horizontal position of the points is given by the generator level y average of the MC events in each bin.

ZEUS 1993+1994

Figure 5: Differential CC cross section versus y for $Q^2 > 200\,\text{GeV}^2$, a) for $x < 0.1$ and b) for $x > 0.1$. The filled (open) dots and the solid (dashed) curves represent the measured values and the Standard Model (SM) prediction of $d\sigma/dy$ for e^+p (e^-p) collisions. The error bars indicate the statistical and systematic uncertainties combined in quadrature. The horizontal position of the points is given by the generator level y average of the MC events in each bin.
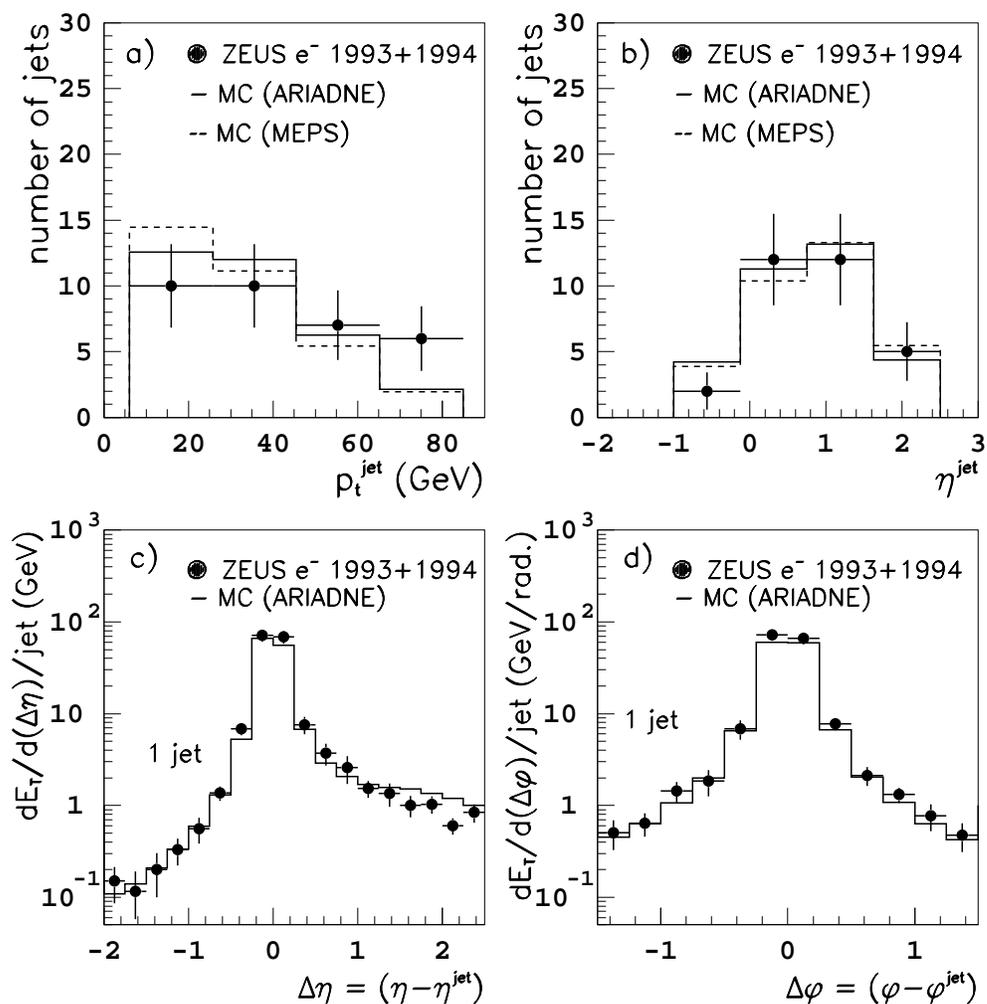
ZEUS 1994
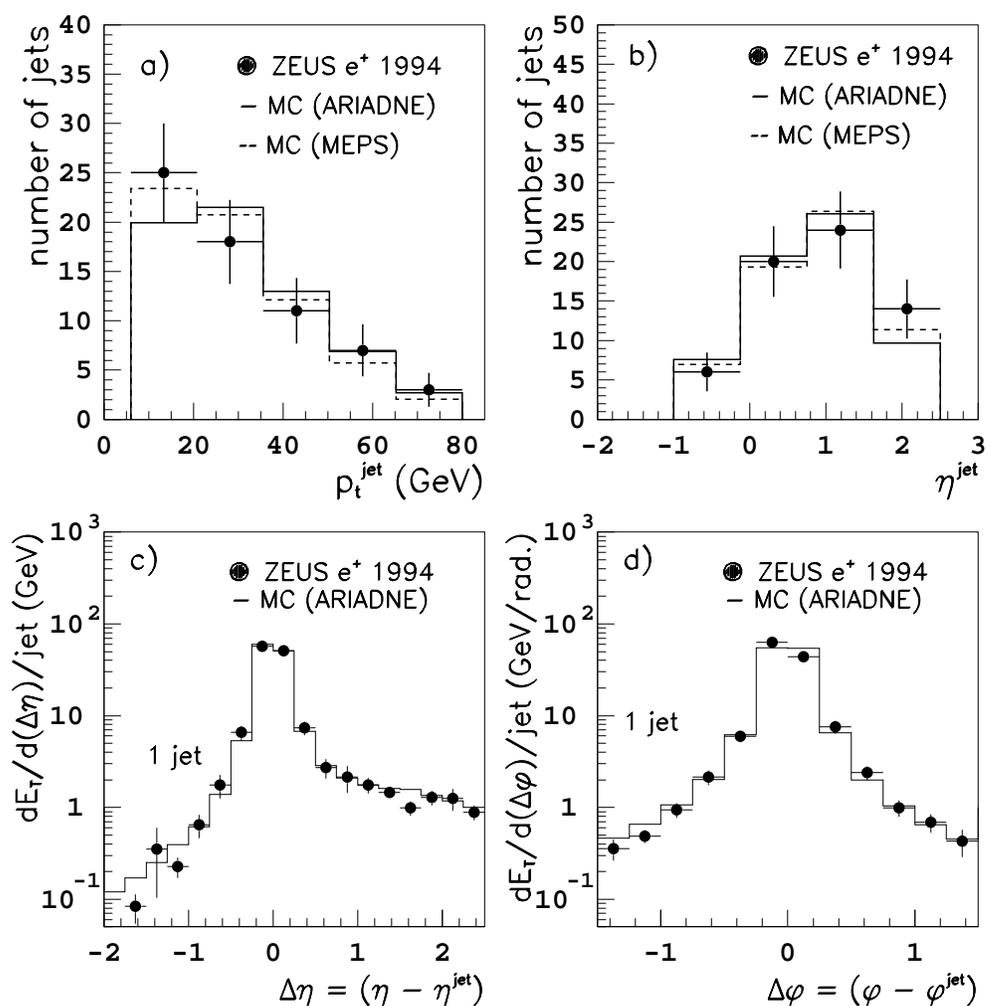
Figure 6: Plots a) and b) show the distributions of transverse momenta and pseudora-pidities of all jets found in the e^+p sample. Plots c) and d) give the transverse energy profiles in η and ϕ for jets in events with exactly one jet. Positive $\Delta\eta$ values correspond to angles between the jet axis and the forward direction. The points denote the data and the solid (dashed) histograms represent the ARIADNE (MEPS) Monte Carlo predictions including detector effects. In plots a) and b) the MC predictions have been normalized to the number of jets observed in the data.

Figure 7: Plots a) and b) show the distributions of transverse momenta and pseudorapidities of all jets found in the e^-p sample. Plots c) and d) give the transverse energy profiles in η and ϕ for jets in events with exactly one jet. Positive $\Delta\eta$ values correspond to angles between the jet axis and the forward direction. The points denote the data and the solid (dashed) histograms represent the ARIADNE (MEPS) Monte Carlo predictions including detector effects. In plots a) and b) the MC predictions have been normalized to the number of jets observed in the data.
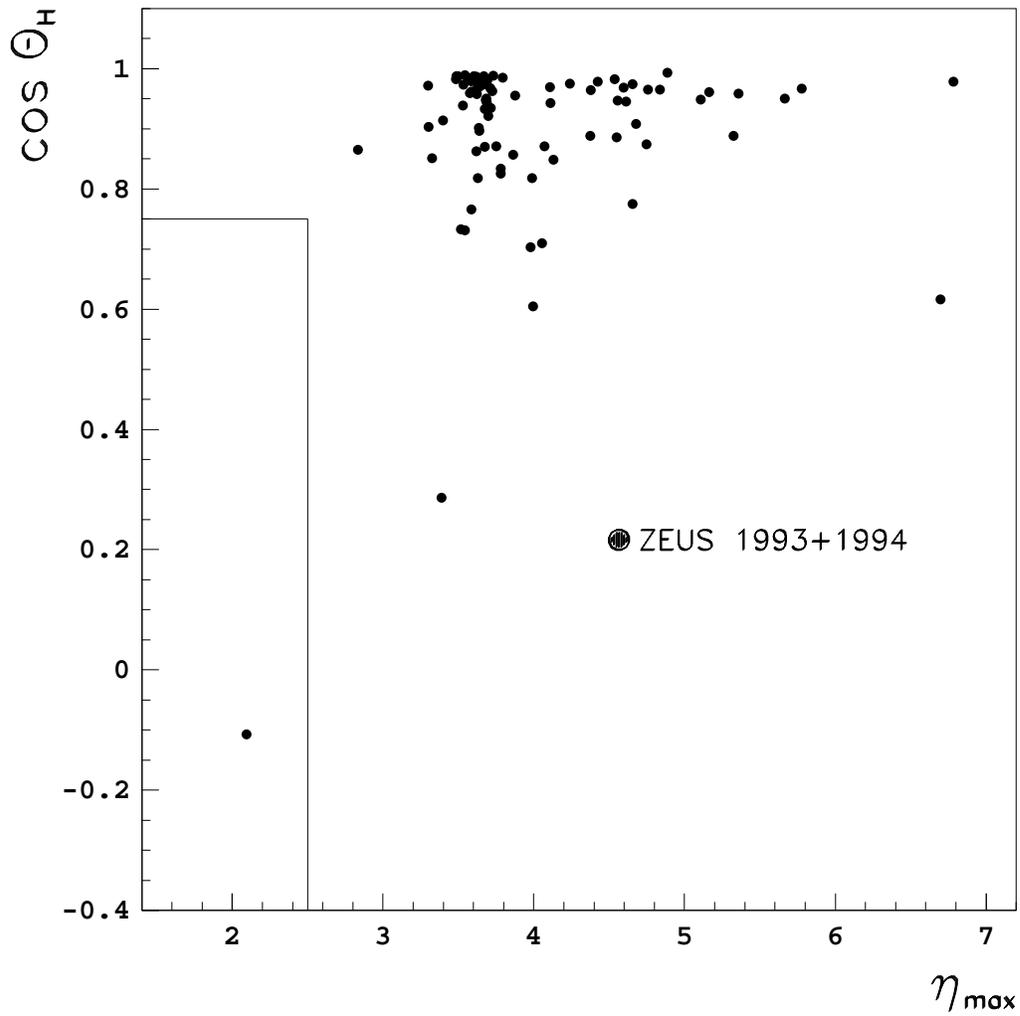
Figure 8: Scatter plot of $\cos\theta_H$ vs. $\eta_{\max}$ containing all events in both the e^+p and the e^-p samples (see section 5.3 for the definitions of θ_H and $\eta_{\max}$). The region $\cos\theta_H < 0.75$ and $\eta_{\max} < 2.5$, which corresponds to large rapidity gap events, contains a single event.
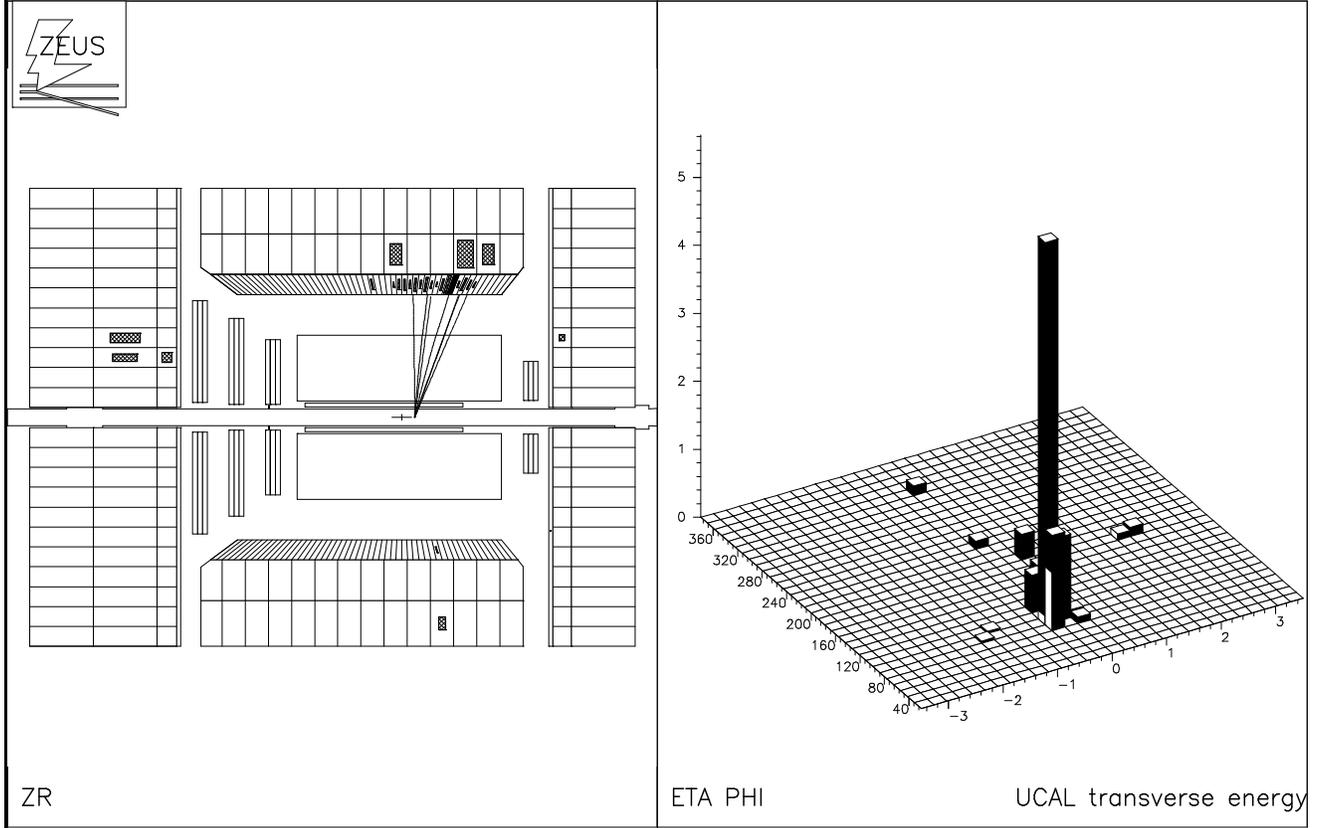
Figure 9: A display of the candidate large rapidity gap event. The left part shows the ZEUS inner tracking system and the calorimeter. The proton beam enters from the right; correspondingly, FCAL, BCAL and RCAL are displayed from left to right. The filled rectangles in the calorimeter denote energy deposits which are above the noise thresholds described in the text (cf. section 3.1) and in addition are above 100 MeV if they are isolated. The ZR–view shows a projection of tracks and energy deposits along constant values of Z and $R = (X^2 + Y^2)^{1/2}$, where the two hemispheres are separated by a plane perpendicular to the event sphericity axis ($20° < \phi < 200°$ corresponding to the upper half of the display). In the right part of the figure the η–ϕ–distribution of the calorimeter transverse energy is presented. The FCAL cluster at $\eta = 2.2$ has $0.25\,\mathrm{GeV}$ of transverse momentum. The kinematic variables for this event are reconstructed to be $\displaystyle{\not}P_t$=14$\pm$2 GeV, Q^2=300 $\pm$ 70 GeV^2, x=0.0093 $\pm$ 0.0015 and y=0.35 $\pm$ 0.10.

34